ESC European Society of Cardiology

Cardiovascular Research (2024) **120**, 1385–1399
https://doi.org/10.1093/cvr/cvae131

Macrophage-derived FGFR1 drives atherosclerosis through PLCγ-mediated activation of NF-κB inflammatory signalling pathway

Lintao Wang[1,2,3], Wu Luo[1,4], Suya Zhang[3], Junsheng Zhang[5,6], Lu He[3], Yifan Shi[2], Li Gao[3,5], Baochuan Wu[2], Xiaoyan Nie[3], Chenghong Hu[1,4], Xue Han[1], Chaoyong He[3]*, Biao Xu [2]*, and Guang Liang [1,4]*

[1]Department of Pharmacy and Institute of Inflammation, Zhejiang Provincial People's Hospital, Affiliated People's Hospital, Hangzhou Medical College, Shangtang Road 158, Hangzhou, Zhejiang 310014, China; [2]Department of Cardiology, Nanjing Drum Tower Hospital, State Key Laboratory of Pharmaceutical Biotechnology, Affiliated Hospital of Medical School, Nanjing University, Zhongshan Road 321, Nanjing, Jiangsu 210008, China; [3]State Key Laboratory of Natural Medicines, Department of Pharmacology, China Pharmaceutical University, Longmian Avenue 639, Nanjing, Jiangsu 210009, China; [4]Department of Cardiology, The Affiliated First Hospital of Wenzhou Medical University, Nanbaixiang Street, Wenzhou, Zhejiang 325035, China; [5] Department of Pathology, The First Affiliated Hospital of Anhui Medical University, Hefei, Anhui 230032, China; and [6]Department of Pathology, Anhui Public Health Clinical Center, Hefei, Anhui 230032, China

Received 16 January 2024; revised 22 April 2024; accepted 4 May 2024; online publish-ahead-of-print 6 June 2024

Time of primary review: 14 days

Aims Atherosclerosis (AS) is a leading cause of cardiovascular morbidity and mortality. Atherosclerotic lesions show increased levels of proteins associated with the fibroblast growth factor receptor (FGFR) pathway. However, the functional significance and mechanisms governed by FGFR signalling in AS are not known. In the present study, we investigated fibroblast growth factor receptor 1 (FGFR1) signalling in AS development and progression.

Methods and results Examination of human atherosclerotic lesions and aortas of *Apoe*$^{-/-}$ mice fed a high-fat diet (HFD) showed increased levels of FGFR1 in macrophages. We deleted myeloid-expressed *Fgfr1* in *Apoe*$^{-/-}$ mice and showed that *Fgfr1* deficiency reduces atherosclerotic lesions and lipid accumulations in both male and female mice upon HFD feeding. These protective effects of myeloid *Fgfr1* deficiency were also observed when mice with intact FGFR1 were treated with FGFR inhibitor AZD4547. To understand the mechanistic basis of this protection, we harvested macrophages from mice and show that FGFR1 is required for macrophage inflammatory responses and uptake of oxidized LDL. RNA sequencing showed that FGFR1 activity is mediated through phospholipase-C-gamma (PLCγ) and the activation of nuclear factor-κB (NF-κB) but is independent of FGFR substrate 2.

Conclusion Our study provides evidence of a new FGFR1–PLCγ–NF-κB axis in macrophages in inflammatory AS, supporting FGFR1 as a potentially therapeutic target for AS-related diseases.

* Corresponding authors. Tel/fax: +86 0577 86699396, E-mail: wzmcliangguang@163.com (G.L.); Tel/fax: +86 025 68182812, E-mail: xubiao62@nju.edu.cn (B.X.); Tel: +86 13611597442, E-mail: chaoyonghe@126.com (C.H.)

Graphical Abstract

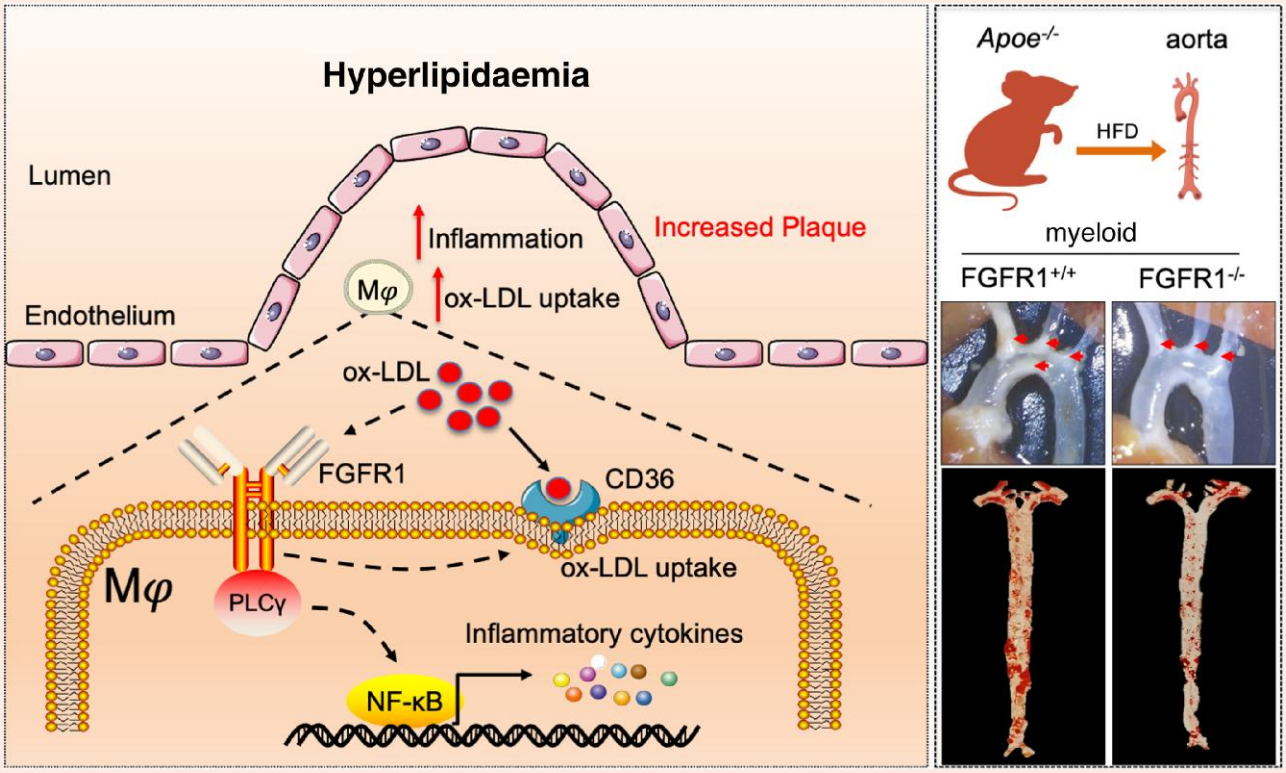

Keywords Atherosclerosis • FGFR1 • Nuclear factor-κB • Macrophage • Inflammation • Oxidized LDL

1. Introduction

Atherosclerosis (AS) is a chronic inflammatory disease that results in aberrant lipid accumulation in major arteries and is the main cause of cardiovascular morbidity and mortality.[1–3] This vasculopathy is characterized by smooth muscle cell (SMC) hyperplasia, endothelial cell alterations, macrophage infiltration, and lipid accumulation in the subendothelial space. These changes occur during a multistep process.[4] The early phase of atherogenesis relies on vascular endothelial cells undergoing inflammatory activation, allowing monocytes to enter the atheroma. Monocyte differentiation into tissue macrophages and internalization of lipoproteins allows these inflammatory cells to generate into foam cells and secrete inflammatory cytokines. Macrophage death creates a necrotic core, destabilizing the plaque and potentially leading to rupture. Therefore, inflammatory reactions dictate both the early and late phases of AS and are responsible for plaque destabilization and the resulting myocardial infarction, stroke, and other cardiovascular complications.[5,6]

Fibroblast growth factor receptor 1 (FGFR1), a member of receptor tyrosine kinase family, has been implicated in a range of activities from growth, development, and carcinogenesis.[7–9] Small-molecule inhibitors of FGFR1 are approved for clinical use for cancer treatment.[10–13] Recently, activation of the FGFR1 signal pathway has been implicated in a host of chronic inflammatory diseases, including inflammatory cardiovascular diseases.[14–17] Blockade of FGFR1 signalling pathway by selective inhibitors or genetic silencing also protects against lipopolysaccharide-induced systemic inflammation.[18–20] Studies have revealed that fibroblast growth factor 1 (FGF1)[21,22] and FGF2[21] are expressed primarily in macrophages and SMCs, in both early and late atherosclerotic lesions. These two cell types also express FGFR1 in both simple and advanced lesions.[23] These observations suggest a potential involvement of FGFR1 in human atherogenesis. Indeed, treatment of *Apoe*-deficient mice fed a high-fat diet (HFD) with a non-selective fibroblast growth factor receptor (FGFR) inhibitor SU5402 showed significant reduction in neointima growth.[24] Notwithstanding the important results, SU5402 is known to inhibit FGFR1–4 and other kinases, including mitogen-activated protein kinases, vascular endothelial growth factor signalling, and platelet derived growth factor signalling. Therefore, this potential involvement as well as the mechanisms by which FGFR1 regulates inflammatory AS remains largely unknown. Detailed investigation of the role of FGFR1 in AS is needed.

In the present study, we examined FGFR1 in aortas of *Apoe*$^{-/-}$ mice fed a HFD and found that CD68-positive macrophages express FGFR1. We then knocked out *Fgfr1* in *Apoe*$^{-/-}$ mice using myeloid-exclusive expression of lysozyme C (LysM) and showed that these *Fgfr1*-deficent mice are largely protected against HFD-induced atherosclerotic lesions. Both *in vitro* and *in vivo* studies show that oxidized low-density lipoprotein (ox-LDL)–mediated activation and inflammatory factor expression in macrophages depend on FGFR1. Mechanistically, FGFR1 links ox-LDL to nuclear factor kappa B (NF-κB) through phospholipase-C-gamma (PLCγ) but not the typical FGFR substrate 2 (FRS2). Our study has provided new fundamental insight into macrophage FGFR1–PLCγ–NF-κB axis in AS.

2. Methods

2.1 Reagents and cells

FGFR1 inhibitor AZD4547[25] was obtained from Shanghai Kaiyu Pharmatech Technology Co. Ltd (Shanghai, China) and was dissolved in dimethyl sulfoxide for *in vitro* experiments and 1% sodium carboxyl methyl

cellulose (CMC-Na) for *in vivo* experiments. Human ox-LDL (cat#YB-002) and DiI (3,3′-dioctadecylindocarbocyanine)-labelled ox-LDL (cat# YB-0010) were obtained from Yiyuan Biomedical Technologies (Guangzhou, China). Antibodies against glyceraldehyde 3-phosphate dehydrogenase (GAPDH; cat# 2118), FGFR1 (cat# 9740), PLCγ (cat# 2822), phosphorylated (p−) PLCγ (Y783; cat# 2821), NF-κB p65 (NF-κB; cat# 8242), p-NF-κB p65 (S536; cat# 3033), and VCAM-1 (cat# 39036) were purchased from Cell Signaling Technology (Danvers, MA, USA). Antibodies against phosphorylated FGFR1 (Y654; cat# ab59194), FRS2 (cat# ab137458), p-FRS2 (Y436; cat# ab193363), α-smooth muscle actin (α-SMA; cat# ab124964), CD68 (cat# ab303565), and Ki67 (cat# 15580) were purchased from Abcam (Cambridge, MA, USA). Antibody against clathrin heavy chain (cat# sc-271178) was purchased from Santa Cruz Technology (Dallas, TX, USA). Antibodies against α-tubulin (cat# 11224-1-AP) and ApoB (cat# 20578-1-AP) were purchased from Proteintech Group (Rosemont, IL, USA). Antibody against monocyte/macrophage MOMA2 (cat# MCA519G) was purchased from Bio-Rad Laboratories (Hercules, CA, USA). Allophycocyanin (APC)-conjugated anti-CD45R/B220 (cat# 103211), Phycoerythrin (PE)-conjugated anti-CD11b (cat# 101207), and Brilliant Violet 421–conjugated Ly6C (cat# 128031) were purchased from BioLegend (San Diego, CA). PE/Cyanine7-conjugated anti-Ly6G/Ly6C (Gr1; E-AB-F1120H) was purchased from Elabscience Biotechnology Co. Ltd (Wuhan, China). Rabbit IgG (cat# AC042) and mouse IgG isotype controls (cat# AC011) were purchased from ABclonal Technology Co. Ltd (Wuhan, China).

Oil Red O staining kit and assay kits for total cholesterol (TCH; cat# A111-1-1), triglyceride (TG; cat# A110-1-1), LDL-cholesterol (LDL-C; cat# A113-1-1), and high-density lipoprotein-cholesterol (HDL-C; cat# A112-1-1) were purchased from Nanjing Jiancheng Bioengineering Institute (Nanjing, China).

Mouse primary peritoneal macrophages (MPMs) were prepared from C57BL/6J mice as described previously.[26] In brief, C57BL/6J mice received an intraperitoneal injection of 6% thioglycollate solution (0.3 g beef extract, 1 g tryptone, and 0.5 g sodium chloride dissolved in 100 mL ddH_2O) and were kept in a pathogen-free condition for 3 days. Total MPMs were harvested by washing the peritoneal cavity with RPMI-1640 medium and centrifuging and suspending the samples in RPMI-1640 medium supplemented with 10% foetal bovine serum, 100 U/mL penicillin, and 100 mg/mL streptomycin. RAW264.7 cells were obtained from the Shanghai Institute of Biochemistry and Cell Biology (Shanghai, China) and cultured in Dulbecco's Modified Eagle's Medium (Thermo Fisher, Waltham, MA) containing 4.5 g/L glucose and 10% foetal bovine serum (Thermo Fisher), and 1× antibiotic-antimycotic (Thermo Fisher).

2.2 Human coronary artery sample analysis

The study was approved by the Clinical Pathology Center of the First Affiliated Hospital of Anhui Medical University (approval no. 2023188) and followed the Declaration of Helsinki. Each patient's lineal consanguinity provided written informed consent. Autopsy specimens were obtained. Atherosclerotic coronary artery samples were from patients who had died from multiple organ failure or acute pulmonary oedema. AS was confirmed by histopathology. Non-atherosclerotic (Non-AS) human coronary artery samples were obtained from individuals who had died from industrial injury or unexpected accident, with no histopathological determination of AS. Sample details are provided in Supplementary material online, *Table S1*.

2.3 Mouse AS studies

Apoe$^{-/-}$ mice (strain: 002052) were purchased from the Jackson Laboratory (Bar Harbor, ME, USA). *Fgfr1*$^{f/f}$ mice (strain: T052281) and *Lysozyme 2* Cre mice (*LysM-Cre*; strain: T055107) were purchased from GemPharmatech Co. Ltd (Nanjing, China). We crossbred *LysM-Cre*$^{+/-}$ mice with *Fgfr1*$^{f/f}$ mice to obtain *Fgfr1*$^{f/+}$*LysM-Cre*$^{+/-}$ and *Fgfr1*$^{f/+}$*LysM-Cre*$^{-/-}$ mice. Then, we bred *Fgfr1*$^{f/+}$*LysM-Cre*$^{+/-}$ mice with *Fgfr1*$^{f/+}$*LysM-Cre*$^{-/-}$ mice to generate myeloid-specific *Fgfr1*-deficient mice (*Fgfr1*$^{f/f}$*LysM-Cre*$^{+/-}$, abbreviated here as *Fgfr1*^{CKO}). Subsequently, *Apoe*$^{-/-}$ mice were crossed with *Fgfr1*^{CKO} mice to obtain *Apoe*$^{+/-}$*Fgfr1*$^{f/+}$*LysM-Cre*$^{+/-}$ and *Apoe*$^{+/-}$*Fgfr1*$^{f/+}$*LysM-Cre*$^{-/-}$ mice. Next, we bred *Apoe*$^{+/-}$*Fgfr1*$^{f/+}$*LysM-Cre*$^{+/-}$ mice with *Apoe*$^{+/-}$*Fgfr1*$^{f/+}$*LysM-Cre*$^{-/-}$ mice to generate myeloid-specific *Fgfr1*-deficient *Apoe*$^{-/-}$ mice (*Apoe*$^{-/-}$*Fgfr1*$^{f/f}$*LysM-Cre*$^{+/-}$; abbreviated here as double knockout, DKO). The littermates *Apoe*$^{-/-}$*Fgfr1*$^{f/f}$*LysM-Cre*$^{-/-}$ are abbreviated as AKO-F mice and *Apoe*$^{-/-}$*Fgfr1*$^{+/+}$*LysM-Cre*$^{+/-}$ are abbreviated as AKO-L mice. Genotyping was performed by polymerase chain reaction (PCR), using tail samples and primers listed in Supplementary material online, *Table S2*. PCR bands were separated using 1% agarose gel electrophoresis. Mice were housed at a constant room temperature with a 12:12 h light–dark cycle and fed a standard rodent diet. All animal care and experimental procedures were approved by the China Pharmaceutical University Animal Policy and Welfare Committee (approval no. 2020-11-007). Studies were performed in accordance with the guidelines from Directive 2010/63/EU of the European Parliament.

To induce atherosclerotic lesions, 8-week-old male AKO-F, AKO-L, and DKO mice were fed a HFD containing 21.2% fat and 0.2% cholesterol (TROPHIC Animal Feed High-tech Co. Ltd, Nantong, China; cat# TP26300) for 12 weeks. We also performed studies in female mice to assess the impact of sex in FGFR1-mediated AS using the same experimental schedule. In addition, to assess spontaneous atherosclerotic lesions in *Apoe*$^{-/-}$ mice, we fed male AKO-F and DKO mice with a normal diet (ND) containing 5% fat and 0% cholesterol (TROPHIC Animal Feed High-tech Co. Ltd, Nantong, China; cat# TP26322) for 52 weeks.

To confirm the role of FGFR1 in AS generation, we utilized a pharmacological FGFR1 inhibition model. For this, male *Apoe*$^{-/-}$ mice were randomly divided into three weight-matched groups: mice fed a ND (ND), mice fed a HFD (HFD), and mice fed a HFD and treated with 10 mg/kg AZD4547 every second day (HFD + AZD). In addition, male DKO mice were randomly divided into two weight-matched groups: mice fed a HFD (DKO) and mice fed a HFD and treated with 10 mg/kg AZD4547 every second day (DKO + AZD). AZD4547 was given by gavage for the entire 12-week period. Control for AZD4547 consisted of 1% CMC-Na solution alone.

For all studies, body weights were recorded weekly. Mice were anaesthetized by isoflurane inhalation (1.5%) and then euthanized by cervical dislocation, and the blood and aortas were collected. Aortic tissues were embedded in 4% paraformaldehyde for histological analysis or snap-frozen in liquid nitrogen for Oil Red O staining and gene and protein expression studies. Blood samples were used for determination of lipids, including total TG, HDL- and LDC-C, and TCH.

2.4 Histological analysis of atherosclerotic lesions

For analysis of plaque lesions in aortic sinus, the heart and proximal aorta were removed and embedded in optimum cutting temperature compound. Serial 8 μm thick cryosections were prepared from the middle portion of the ventricle to the aortic arch. Sections were stained with Oil Red O. To do this, sections were fixed in 10% formalin for 10 min and then incubated in 100% propylene glycol for 10 min at room temperature. Sections were incubated with Oil Red O solution for 10 min. A 60% propylene glycol solution was added for 1 min. Nuclei were stained in haematoxylin. For en face analyses, whole aorta was dissected out, opened longitudinally from heart to the iliac arteries, and stained with Oil Red O.

2.5 Tissue immunostaining

For chromogen staining, 8 μm thick sections were deparaffinized, hydrated, and subjected to heat induced antigen retrieval (0.01 M sodium citrate buffer, pH = 6.0). Slides were blocked with 3% hydrogen peroxide for 10 min and in 1% bovine serum albumin for 30 min. Primary antibody incubations were carried out overnight at 4°C (p-FGFR, FGFR1; 1:200). Horseradish peroxidase–conjugated secondary antibody (1:500) and DAB were used for detection. The specificity of FGFR1 immunohistochemical staining was determined by IgG isotype antibody and by using aortic lesions from

DKO mice. ImageJ analysis software version 1.53i (NIH; Bethesda, MD, USA) was used to determine staining-positive area.

For immunofluorescence staining, frozen section slides were fixed in cold methanol and permeabilized using 0.3% Triton X. Slides were then blocked using 5% bovine serum albumin for 30 min and incubated overnight with primary antibodies (CD68, FGFR1, p-NF-κB p65, MOMA2, and Ki67, all at 1:200). Negative control consisted of IgG isotype antibody or no primary antibody. Sections were washed three times with phosphate buffered saline (PBS) and then incubated with appropriate Alexa Fluor 488-, 594-, or 647-conjugated secondary antibodies (1:500) for 1 h at room temperature. Slides were counterstained with DAPI (cat# P36935, Thermo Fisher).

2.6 Flow cytometry

Blood samples collected from mice were used for the analysis of leucocyte subsets. Forward scatter and side scatter were used to gate live cells, excluding red blood cells, debris, and cell aggregates. Myeloid cells were identified as $CD11b^+$. Monocytes were identified as $CD11b^+$ $Ly6G^-$. Classical monocytes were measured as $Ly6C^{high}$ and non-classical monocytes as $Ly6C^{low}$. Neutrophils were identified as $CD11b^+Ly6G^+$. For these determinations, antibodies included APC-conjugated anti-CD45R/B220, PE-conjugated anti-CD11b, PE/Cyanine7-conjugated anti-Ly6G/Ly6C (Gr1), and Brilliant Violet 421–conjugated anti-Ly6C. Flow cytometry was performed in BD FACSAria™ III (BD Bioscience, USA).

Mouse aortic cells were obtained from enzymatic dissociation using tissue digestion containing 1 mg/mL collagenase I, 1 mg/mL collagenase II, and 100 μg/mL DNase I. Fixable viability dye (eBioscience, cat#65-0865-14) was used for screening live cells. Myeloid cells were identified as $CD11b^+$. Monocytes were identified as $CD11b^+Ly6G^-$. Classical monocytes were measured as $Ly6C^{high}$ and non-classical monocytes as $Ly6C^{low}$. Neutrophils were identified as $CD11b^+Ly6G^+$. Flow cytometry was performed in BD FACSAria™ III (BD Bioscience, USA).

2.7 Real-time quantitative PCR

Total RNA was isolated from cells and mouse tissues using TRIzol reagent (Invitrogen). Reverse transcription and quantitative PCR (qPCR) were carried out using a two-step M-MLV Platinum SYBR Green qPCR SuperMix-UDG kit (Thermo Fisher) in Eppendorf Mastercycler Realplex detection system (Eppendorf, Hamburg, Germany). Primers were obtained from Thermo Fisher (Shanghai, China). Primer sequences are listed in Supplementary material online, *Table S3*. mRNA levels of target genes were normalized to *Actb*.

2.8 RNA-seq and single-cell RNA-seq analysis

MPMs isolated from $Fgfr1^{f/f}$ and $Fgfr1^{CKO}$ mice were challenged with 50 μg/mL ox-LDL for 12 h. Total RNA of MPMs, with or without ox-LDL challenge, was prepared with TRIzol reagent (Invitrogen), and RNA-seq was performed by Majorbio Technology Inc. (Shanghai, China). For data analysis, differentially expressed genes (DEGs) that showed four-fold alteration were identified by using *P*-adjust 0.05 as cut-off. Venn analysis, KEGG enrichment analysis, volcano analysis, and GSEA analysis were performed with online software (http://geneontology.org/). The DEGs in the highlighted KEGG pathway are listed in Supplementary material online, *Table S5*. DEGs used in KEGG analysis were the intersection of the genome $Fgfr1^{f/f}$ vs. $Fgfr1^{f/f}$ + ox-LDL and the genome $Fgfr1^{f/f}$ + ox-LDL vs. $Fgfr1^{CKO}$ + ox-LDL listed in Supplementary material. All DEGs in the genome $Fgfr1^{f/f}$ vs. $Fgfr1^{f/f}$ + ox-LDL and the genome $Fgfr1^{f/f}$ + ox-LDL vs. $Fgfr1^{CKO}$ + ox-LDL are listed in Supplementary material, respectively.

For scRNA-seq, GSE214414 data sets were used. Top 2000 highly variable genes were calculated using the Seurat function FindVariableGenes (mean.function = FastExpMean, dispersion.function = FastLogVMR). Principal component analysis (PCA) was performed to reduce the dimensionality with RunPCA function. Graph-based clustering was performed to cluster cells according to the gene expression profile with the FindClusters function. Cells were visualized using a two-dimensional Uniform Manifold Approximation and Projection (UMAP) algorithm with the RunUMAP function. The FindAllMarkers function (test.use = presto) was used to identify marker genes of each cluster. DEGs were selected using the function FindMarkers (test.use = presto). A $P < 0.05$ and $|\log2\text{fold-change}| > 0.58$ were set as the threshold for significantly differential expression. The sequencing and bioinformatics analysis were provided by OE Biotech Co. Ltd (Shanghai, China).

2.9 Western immunoblotting

Lysates from cultured cells and mouse tissues were prepared and protein concentrations determined by the Bradford assay (Bio-Rad Laboratories, Hercules, CA). Proteins were separated using 10% sodium dodecyl sulfate (SDS)–polyacrylamide gel electrophoresis and electro-transferred to nitrocellulose membranes. Membranes were then blocked for 1.5 h at room temperature in Tris-buffered saline (pH 7.6) containing 0.05% Tween 20 and 5% non-fat dry milk. Primary antibody incubations were carried out at 4°C overnight. Secondary antibodies were applied for 1 h at room temperature. Immunoreactivity was visualized using enhanced chemiluminescence reagents (Bio-Rad Laboratories). Densitometric measurements were made using ImageJ. Representative blots are shown in the figures. All experiments were performed a minimum of three different times with three-plus replicates at each time point.

2.10 Immunoprecipitation

Cell lysates were pre-cleared with protein A/G magnetic beads to remove proteins binding to the beads, and part of the lysate was retained as an input sample. Then, the protein lysate was incubated with the corresponding primary antibody overnight at 4°C. As a negative control (NC), equal amount of IgG isotype antibody was used. Samples were precipitated with protein A/G magnetic beads for 0.5 h at 4°C. Precipitated proteins were washed with ice cold lysis buffer for three times, and then, the washed protein G Sepharose beads were resuspended in a loading buffer containing SDS and then subjected to heat denaturation for 10 min at 100°C for subsequent immunoblotting. Immunoblotting studies were repeated at least three times with different samples. Bands were quantified using ImageJ software.

2.11 Gene silencing in cell cultures

Gene silencing in cells was achieved using siRNA. siRNAs targeting *Plcg1*, *Frs2*, and control (scrambled; NC) were purchased from GenePharma Co. Ltd (Shanghai, China). Sequences are shown in Supplementary material online, *Table S4*. RAW264.7 cells were incubated with siRNA using Lipofectamine 2000 (Thermo Fisher). Knockdown was confirmed by immunoblotting.

2.12 Ox-LDL uptake, signalling, and lipid accumulation

To investigate downstream signalling in response to ox-LDL, MPMs, harvested from $Fgfr1^{f/f}$ and $Fgfr1^{CKO}$ mice, were incubated in fresh media containing 50 μg/mL ox-LDL for various time points. Western blotting was performed to examine FGFR activation. qPCR and enzyme-linked immunosorbent assay (ELISA) were performed for inflammatory cytokine expression. To study ox-LDL uptake, MPMs harvested from $Fgfr1^{f/f}$ and $Fgfr1^{CKO}$ mice were incubated in fresh media containing 100 μg/mL ox-LDL for 24 h at 37°C. Cells were then fixed with 4% paraformaldehyde for 15 min, washed with PBS, and incubated with a 0.5% working solution of Oil Red O for 15 min. For some studies, labelled 50 μg/mL Dil-ox-LDL was used for 24 h at 37°C. Cells exposed to Dil-ox-LDL were counterstained with DAPI, and fluorescence images were taken.

Where indicated, MPMs harvested from WT mice were pre-treated with 10 μM AZD4547 for 1 h before exposure to 100 μg/mL ox-LDL for Oil Red O staining. For fluorescence imaging studies, cells were pre-treated with AZD4547 and then exposed to 50 μg/mL Dil-ox-LDL for 24 h. Cells were fixed, stained for Clathrin (Alexa Fluor 488 detection), and imaged.

2.13 Inflammatory cytokine determinations

Lysates prepared from tissues and cell culture media were used to measure tumour necrosis factor alpha (TNF-α) and interleukin (IL)-6 protein levels by ELISA (eBioscience, San Diego, CA). The total quantity of the inflammatory factors was normalized to mL media or mg tissue.

2.14 Statistical analysis

All experiments were randomized and blinded. Data are reported as mean ± SEM. Statistical analysis was performed with GraphPad Prism 9.0 software (San Diego, CA, USA). When comparing the difference between two groups, Student's *t*-test (unpaired, two-tailed) was applied. We used one-way analysis of variance (ANOVA) followed by Bonferroni's *post hoc* test when comparing more than two groups of data. *P* values of <0.05 were considered to be statistically significant. Post-tests were run only if *F* achieved $P < 0.05$ and there was no significant variance in homogeneity.

3. Results

3.1 Macrophage FGFR1 is induced in AS

Atherosclerotic lesions were generated in *Apoe*$^{-/-}$ mice through HFD feeding for 12 weeks. We examined FGFR1 protein in atherosclerotic lesions by immunohistochemistry and used phosphorylated FGFR1 as a proxy for receptor activity. Twelve weeks of HFD feeding in *Apoe*$^{-/-}$ mice increased FGFR1 and *p*-FGFR1 (Y654) immunoreactivity in atherosclerotic lesions (*Figure 1A*; Supplementary material online, *Figure S1A*). We then analysed scRNA-seq data (GSE214414) from a study in which aorta tissues of ND-fed wild-type (WT ND) and HFD-fed *Apoe*$^{-/-}$ (*Apoe*$^{-/-}$ HFD) mice were used. We identified various cell types including T cells, B cells, endothelial cells, fibroblasts, macrophages, monocytes, neutrophils, red blood cells, and SMCs, and the expression of FGFR1 was analysed (*Figure 1B*; Supplementary material online, *Figure S1B and C*). The ratio (98.4%) of macrophages in tissues of *Apoe*$^{-/-}$ HFD mice was higher than that (11.1%) in tissues of WT ND mice, and the number of macrophages in tissues of *Apoe*$^{-/-}$ HFD mice was much bigger than monocytes and neutrophils in the myeloid fraction (*Figure 1C*). Furthermore, we found that FGFR1 was expressed on macrophages and monocytes in tissues of *Apoe*$^{-/-}$ HFD mice and only expressed on monocytes in tissues of WT ND mice (*Figure 1D* and *E*). In addition, we can see that the total FGFR1 expression in immune cells in arterial tissues of *Apoe*$^{-/-}$ HFD mice is much more than that in WT ND mice (*Figure 1D* and *E*).

We then performed double-immunofluorescence labelling of aortas of *Apoe*$^{-/-}$ mice fed a ND or HFD for FGFR1 and CD68 as a marker of macrophages. Our results show co-localization of FGFR1 with CD68-positive cells in mouse atherosclerotic lesions (*Figure 1F* and *G*; Supplementary material online, *Figure S2A and B*). These studies suggest that HFD feeding induces infiltration of CD68^{+} macrophages in atherosclerotic lesions and these cells express FGFR1 (*Figure 1F*). To confirm these results in human AS, we examined autopsy specimens from subjects with diagnosed AS and compared the results with non-atherosclerotic samples. As expected from our experimental studies, human AS was associated with an increased level of double positive cells expressing CD68 and FGFR1/p-FGFR1 (*Figure 1H–K*; Supplementary material online, *Figure S2C–E*). These findings show that AS is associated with elevated levels of phosphorylated and total FGFR1, primarily in macrophages.

3.2 Myeloid cell–specific *Fgfr1* deficiency prevents lipid accumulation and atherogenesis in *Apoe*$^{-/-}$ HFD mice

As our studies pointed to elevated macrophage FGFR1 in atherosclerotic lesions, we generated myeloid-specific *Fgfr1* deficiency to examine the functional significance of FGFR1 in AS development and progression. We bred *Fgfr1*-floxed mice with *LysM-Cre* mice. Genotyping and western blot assay confirmed the deletion of *Fgfr1* in these mice (see Supplementary material online, *Figure S3A and B*). We then crossed *Apoe*$^{-/-}$ mice with *Fgfr1*^{CKO} mice to generate *Apoe*$^{-/-}$*Fgfr1*$^{f/f}$ *LysM-Cre*$^{+/-}$ DKO mice and compared them with *Apoe*$^{-/-}$*Fgfr1*$^{f/f}$*LysM-Cre*$^{-/-}$ (AKO-F) and *Apoe*$^{-/-}$*Fgfr1*$^{+/+}$*LysM-Cre*$^{+/-}$ (AKO-L) upon HFD feeding for 12 weeks (*Figure 2A*). We did not find any changes to monocyte and neutrophil numbers in the peripheral blood when AKO-F and DKO mice were fed a HFD (see Supplementary material online, *Figure S3C*). HFD feeding of AKO-L and AKO-F mice led to plaque development along the aorta, while deletion of *Fgfr1* in myeloid cells (DKO) prevented HFD-induced atherosclerotic lesions in aortic arch (*Figure 2B*). *Fgfr1* deficiency in myeloid cells did not change the body weight and serum lipid levels upon HFD feeding for 12 weeks (*Figure 2C–G*). As anticipated, AKO-L and AKO-F mice showed fatty streaks along the length of their aortas as indicated by Oil Red O staining (*Figure 2H* and *I*). Significantly reduced fatty streak and Oil Red O–positive areas were noted in DKO mice. Analysis of aortic roots showed that DKO mice have less lesion areas, necrotic area, and Oil Red O–positive staining than AKO-F or AKO-L mice upon HFD feeding (*Figure 2J–N*). Levels of macrophages and monocytes, marked with MOMA2-stained aortas, showed reduced immunoreactivity in DKO mice (*Figure 2O* and *P*; Supplementary material online, *Figure S4A*). Flow cytometric analysis of the aorta further validated a decrease in CD11b^{+} cells (including the proportional monocytes and neutrophils) in arterial tissues of HFD-fed DKO mice, compared with that in HFD-fed AKO-F mice (see Supplementary material online, *Figure S4B*). However, contractile SMCs showed no changes (see Supplementary material online, *Figure S4C*), which might result from less effects of myeloid *Fgfr1* deletion on SMC phenotypic switching or few plaque instability in 12-week *Apoe*$^{-/-}$ HFD mice.

To determine whether sex is a variable in the involvement of myeloid *Fgfr1* in atherosclerotic plaque development, we analysed tissues from female AKO-F and DKO mice at the same age fed a HFD (*Figure 3A*). We also did not find differences in serum lipid levels between female AKO-F and DKO mice fed a HFD for 12 weeks (*Figure 3B–E*). We found that myeloid *Fgfr1* deficiency significantly reduces atherosclerotic plaques and Oil Red O–stained aortas in female mice (*Figure 3F–H*), like in male mice. Deleting *Apoe* gene has been shown to generate spontaneous AS development in mice with a long-time ND.[27] Specifically, *Apoe*$^{-/-}$ mice show foam cell lesions and fibrous plaques around 20 weeks of age on ND. To examine whether *Fgfr1* deficiency alters spontaneous AS development, we examined tissues of male AKO-F and DKO mice fed a ND for up to 52 weeks (*Figure 3I*). We found that myeloid-specific deficiency of *Fgfr1* protected against spontaneous atherosclerotic plaque formation, without causing any changes to serum lipid levels (*Figure 3J–P*). These findings validate that myeloid-specific FGFR1 participates in aortic plaque formation and atherogenesis in mice.

3.3 Pharmacological inhibition of FGFR1 prevents atherogenesis in *Apoe*$^{-/-}$ mice fed a HFD

We used a selective small-molecule inhibitor of FGFR1, AZD4547,[25,28] in *Apoe*$^{-/-}$ mice to confirm the role of FGFR1 in AS. For these studies, *Apoe*$^{-/-}$ mice were fed a ND or HFD for 12 weeks. A cohort of *Apoe*$^{-/-}$ HFD mice were treated with AZD4547 every other day for the duration of the study (*Figure 4A*). As expected, HFD-induced atherosclerotic plaques, fatty streaks, aortic lesions, Oil Red O staining, and levels of macrophages were reduced in mice treated with AZD4547 (*Figure 4B–J*). α-SMA–stained areas showed no changes in mice treated with AZD4547 (see Supplementary material online, *Figure S5A and B*). AZD4547 treatment did reduce HFD-induced innominate arterial tissue lipid accumulation, atherogenesis, and MOMA2 immunoreactivity in *Apoe*$^{-/-}$ mice fed a HFD (see Supplementary material online, *Figure S5C–H*). Interestingly, AZD4547 treatment also reduced HFD-mediated weight gain in mice and serum lipid levels, possibly indicating lipid metabolism changes in hepatocytes and adipocytes through FGFR1 alteration (see Supplementary material online, *Figure S5I–L*).

We used DKO mice to confirm our studies of FGFR1 pharmacological inhibition. For these studies, DKO mice were fed a HFD for 12 weeks. A HFD experimental group was treated with AZD4547 every other day for

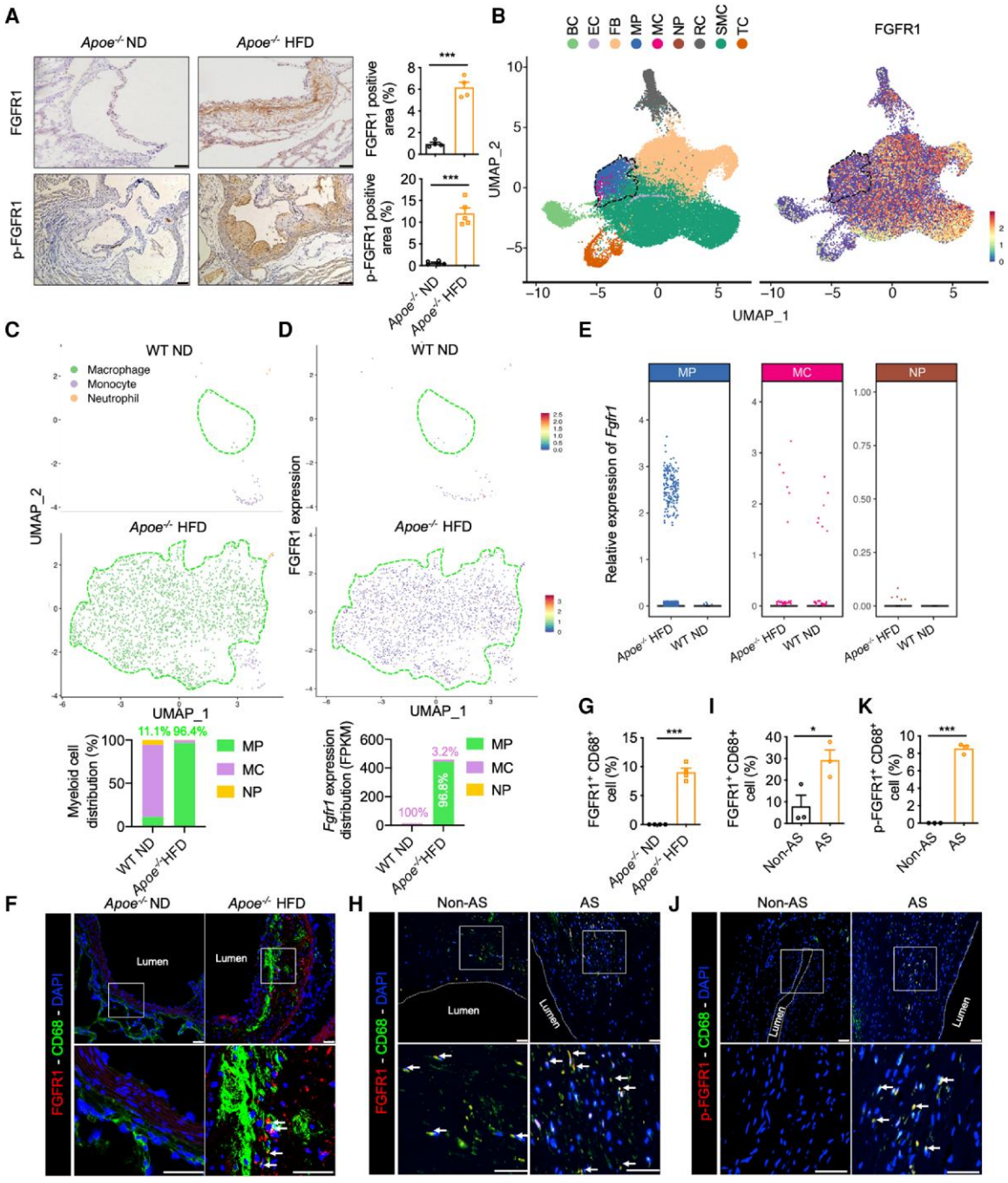

Figure 1 FGFR1 is up-regulated and activated in AS. (*A*) Aortic tissues from *Apoe*$^{-/-}$ mice fed a ND or a HFD for 12 weeks were evaluated for total and p-FGFR1 by immunohistochemical staining. Immunoreactivity was detected by DAB. Tissues were counterstained with haematoxylin (scale bar = 100 μm). Immunoreactivity quantification is shown on the right (mean ± SEM; $n = 4$; ***$P < 0.001$). (*B*) UMAP plot of cell clusters (left) and FGFR1 expression (right) in aortas from WT ND mice and *Apoe*$^{-/-}$ HFD mice (GSE214414). (*C*) UMAP plot of macrophages, monocytes, and neutrophils in aortas of WT ND and *Apoe*$^{-/-}$ HFD mice. The ratios of macrophages, monocytes, and neutrophils are shown. (*D*) UMAP plot of *Fgfr1* expression in aortas of WT ND and *Apoe*$^{-/-}$ HFD mice. Quantification of *Fgfr1* distribution in macrophages, monocytes, and neutrophils is shown. (*E*) Boxplot of *Fgfr1* expression in myeloid cells of WT ND and *Apoe*$^{-/-}$ HFD mice. (*F* and *G*) Aortic tissues from *Apoe*$^{-/-}$ mice fed a ND or a HFD were labelled with FGFR1 and macrophage marker CD68. Tissues were counterstained with DAPI. Representative staining images (*F*) and quantification of positive cells (*G*) are shown (scale bar = 100 μm for upper panel; 30 μm for lower panels; mean ± SEM; $n = 4$; ***$P < 0.001$). (*H* and *I*) Coronary artery tissues from patients with AS and non-AS were evaluated for FGFR1 immunoreactivity. Tissues were also labelled with CD68 and counterstained with DAPI. Representative images are shown in (*H*) [scale bar = 50 μm]. Quantification of immunoreactivity is presented in (*I*) [mean ± SEM; $n = 3$; *$P < 0.05$]. (*J* and *K*) Samples shown in (*H*) and (*I*) were stained for p-FGFR1 and CD68 and counterstained with DAPI. Representative images are shown in (*J*) [scale bar = 50 μm]. Quantification of immunoreactivity is presented in (*K*) [mean ± SEM; $n = 3$; ***$P < 0.001$]. Student's *t*-test (unpaired, two-tailed) for (*A*), (*G*), (*I*), and (*K*). BC, B cell; EC, endothelial cell; FB, fibroblast; MP, macrophage; MC, monocyte; NP, neutrophil; RC, red cell; SMC, smooth muscle cell; TC, T cell.

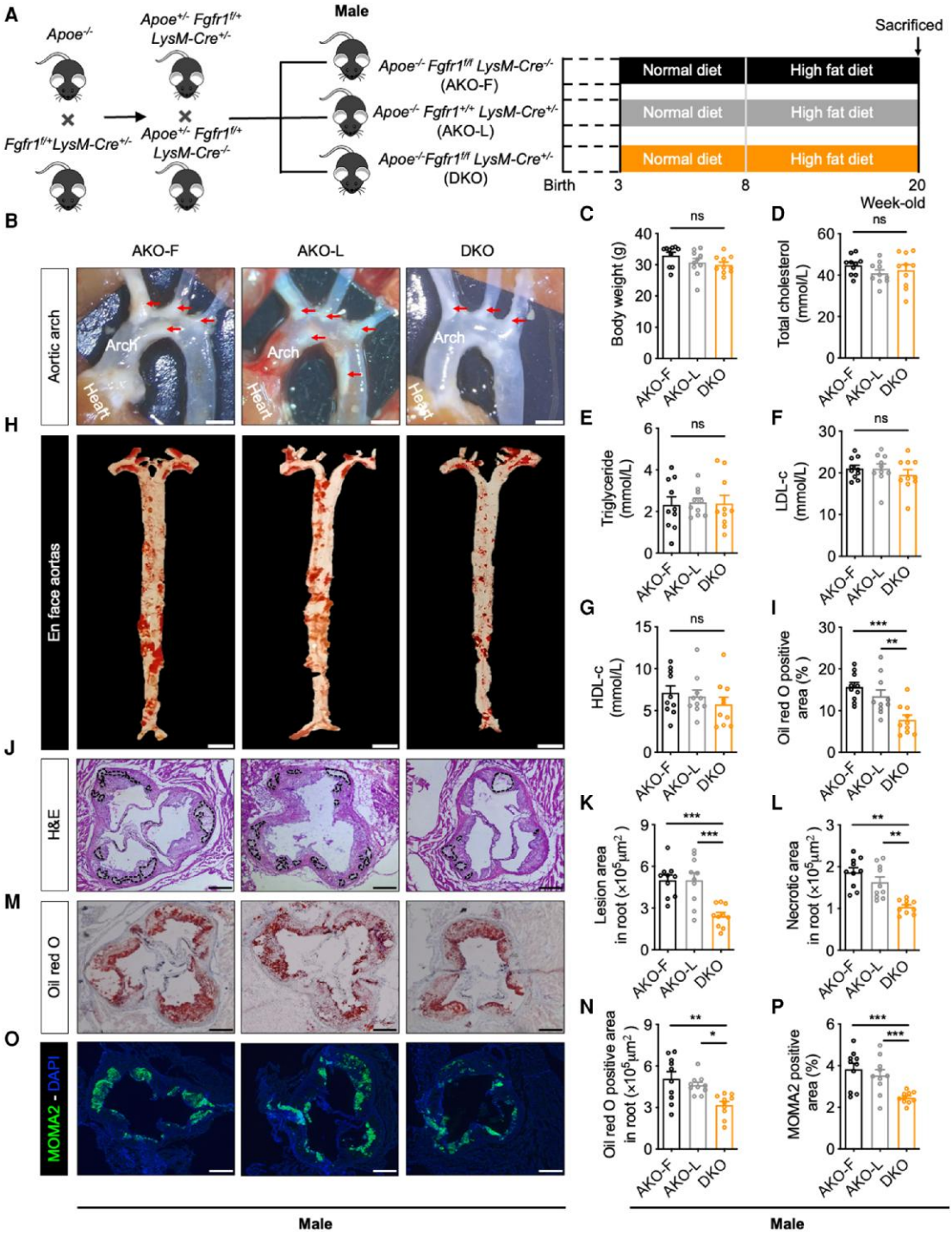

Figure 2 Myeloid-specific *Fgfr1* deficiency reduces atherosclerotic lesions in *Apoe*$^{-/-}$ mice. (*A*) Schematic showing generation of myeloid-specific *Fgfr1*-deficeint *Apoe*$^{-/-}$ mice. For these studies, AKO-F and AKO-L were compared with DKO mice. (*B*) Representative image of aortic arch from male AKO-F, AKO-L, and DKO mice fed a HFD for 12 weeks (scale bar = 1 mm). (*C–G*) Figures showing body weights of mice, TCH, TGs, and LDL- and HDL-C in male AKO-F, AKO-L, and DKO mice fed a HFD for 12 weeks (mean ± SEM; $n = 10$). (*H*) Representative image of Oil Red O staining of en face aortas from male AKO-F, AKO-L, and DKO mice fed a HFD for 12 weeks (scale bar = 2.5 mm). (*I*) Quantification of Oil Red O–stained aortas shown in (*I*) [mean ± SEM; $n = 10$; $^{**}P < 0.01$, $^{***}P < 0.01$]. (*J*) Representative H&E-stained aortic root tissues from male AKO-F, AKO-L, and DKO mice after HFD feeding for 12 weeks (scale bar = 250 μm). (*K* and *L*) Quantification of atherosclerotic plaque area and necrotic area from H&E-stained sections (mean ± SEM; $n = 10$; $^{**}P < 0.01$, $^{***}P < 0.001$). (*M* and *N*) Representative image of Oil Red O staining of aortic root tissue sections (*M*; scale bar = 250 μm). Quantification of Oil Red O staining is shown in (*N*) [mean ± SEM; $n = 10$; $^{*}P < 0.05$, $^{**}P < 0.01$]. (*O* and *P*) Immunostaining of aortic root tissues of male AKO-F, AKO-L, and DKO mice for monocyte/macrophage marker MOMA2. Tissues were counterstained with DAPI (scale bar = 250 μm). Quantification of immunoreactivity is shown in (*P*) [mean ± SEM; $n = 10$; $^{***}P < 0.001$]. One-way ANOVA followed by Bonferroni's *post hoc* test for (*C–G*), (*I*), (*K*), (*L*), (*N*), and (*P*). ns, not significant.

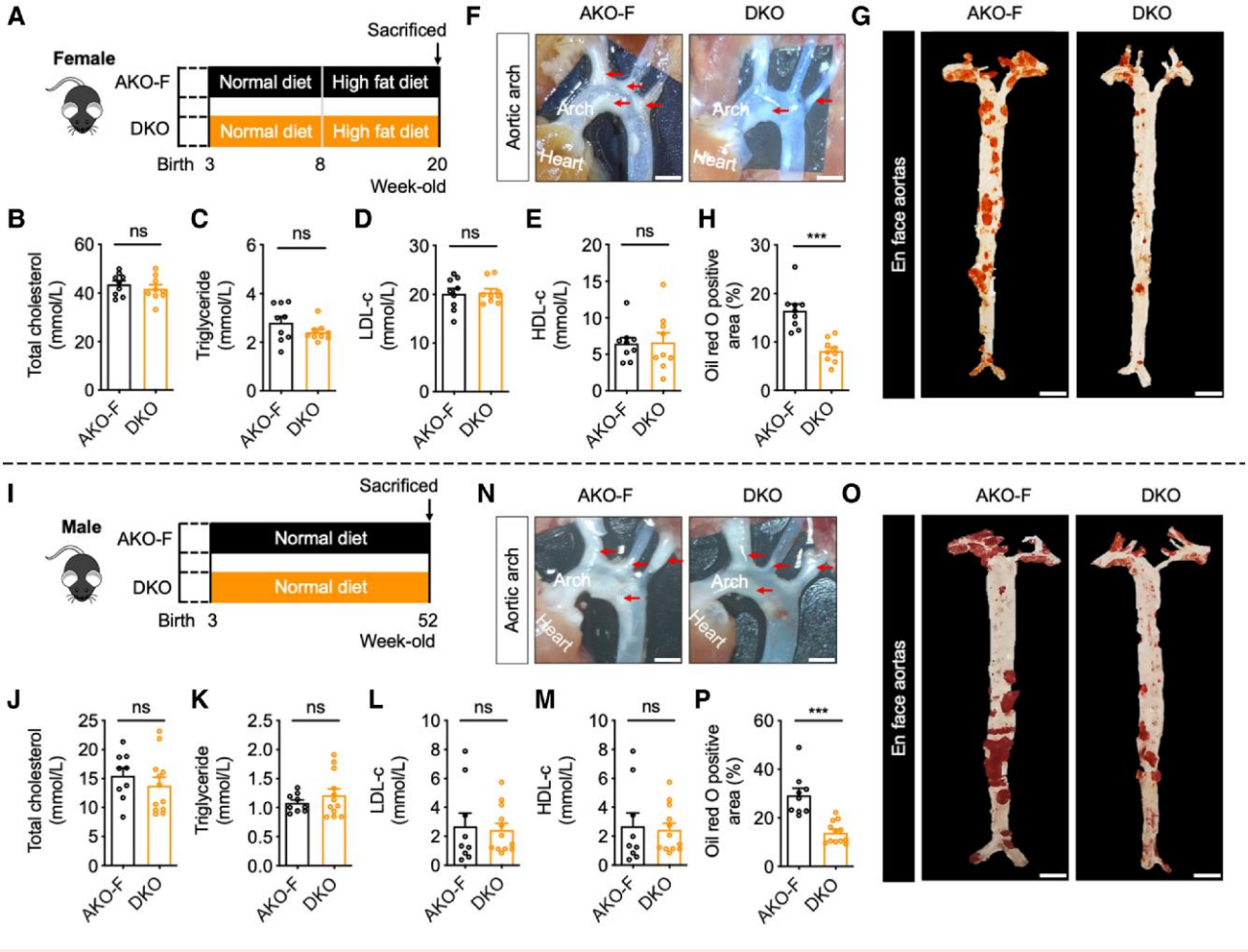

Figure 3 Impact of myeloid-specific *Fgfr1* in lipid accumulation in female mice and spontaneous atherosclerotic lesions. (*A*) Schematic showing experimental groups and design to investigate the impact of myeloid *Fgfr1* deficiency in female *Apoe*$^{-/-}$ mice. (*B–E*) Levels of TCH, TGs, and LDL- and HDL-C in female AKO-F and DKO mice fed a HFD for 12 weeks (mean ± SEM; $n = 9$). (*F*) Representative image showing thoracic aortic arch (ascending aorta, brachiocephalic, left common carotid, left subclavian, and part of the descending aorta) in female AKO-F and DKO mice fed a HFD (scale bar = 1 mm). (*G* and *H*) Representative Oil Red O staining of dissected aortas from mice (*G*) and quantification (*H*) of stained area (scale bar = 2.5 mm; mean ± SEM; $n = 9$; ***$P < 0.001$). (*I*) Schematic showing experimental groups and design to investigate the impact of myeloid *Fgfr1* deficiency on spontaneous atherosclerotic lesion development. Male AKO-F and DKO mice were fed a normal diet for 52 weeks. (*J–M*) Levels of TCH, TGs, and LDL- and HDL-C in male AKO-F and DKO mice fed a ND for 52 weeks (mean ± SEM; $n = 9$–12). (*N*) Representative image showing thoracic aortic arch (ascending aorta, brachiocephalic, left common carotid, left subclavian, and part of the descending aorta) of mice at 52 weeks (scale bar = 1 mm). (*O* and *P*) Representative Oil Red O staining of dissected aortas from mice (*O*) and quantification (*P*) of stained area (scale bar = 2.5 mm; mean ± SEM; $n = 9$–12; ***$P < 0.001$). Student's *t*-test (unpaired, two-tailed) for (*B–E*), (*H*), (*J–M*), and (*P*). ns, not significant.

the duration of the study (see Supplementary material online, *Figure S6A*). We found that AZD4547 treatment reduced body weight in HFD-fed DKO mice (see Supplementary material online, *Figure S6B*). Furthermore, AZD4547 did not alter the course of HFD-induced atherosclerotic plaques, fatty streaks, aortic lesions, necrotic area, Oil Red O positivity, and MOMA2-positive macrophage/monocyte infiltration (see Supplementary material online, *Figure S6C–I*). No changes were seen to α-SMA immunoreactivity following AZD4547 treatment (see Supplementary material online, *Figure S6J*). These findings confirm the contribution of FGFR1 in AS and indicate that pharmacological inhibition of FGFR1 protects against atherosclerotic lipid accumulation and atherogenesis.

3.4 Role of FGFR1 in AS involves modulation of NF-κB inflammatory responses

AS is considered an inflammatory disease, and localized/activated macrophages contribute significantly to disease initiation and progression.[3] Our results showing that *Fgfr1* deficiency in myeloid cells is protective against plaque development likely point to a direct or indirect role of FGFR1 in inflammatory reactions. To gain such an insight, we harvested MPMs from *Fgfr1*$^{f/f}$ and *Fgfr1*^{CKO} mice and then exposed the cells to 50 μg/mL ox-LDL and performed RNA-seq analysis. We compared the gene expression profile among vehicle-treated *Fgfr1*$^{f/f}$ MPMs, *Fgfr1*$^{f/f}$ MPMs exposed to ox-LDL, and *Fgfr1*^{CKO} MPMs exposed to ox-LDL (*Figure 5A*). KEGG enrichment analysis showed that *Fgfr1* deficiency regulated inflammatory signalling pathway–related genes in ox-LDL–challenged MPMs (*Figure 5B*). We then analysed the RNA-seq data to find the potential signalling pathway(s) linking FGFR1 to inflammatory response. We found 588 down-regulated genes and 667 up-regulated genes when comparing ox-LDL-treated *Fgfr1*$^{f/f}$ MPMs with *Fgfr1*^{CKO} MPMs (*Figure 5C*). A GSEA analysis showed significant changes to NF-κB signalling pathway (*Figure 5D*). To validate these results *in vivo*, we measured inflammatory cytokines IL-6 and TNF-α in serum from AKO-F and DKO mice fed a HFD for 12 weeks and showed that the levels are lower in DKO mice (*Figure 5E* and *F*). These circulating

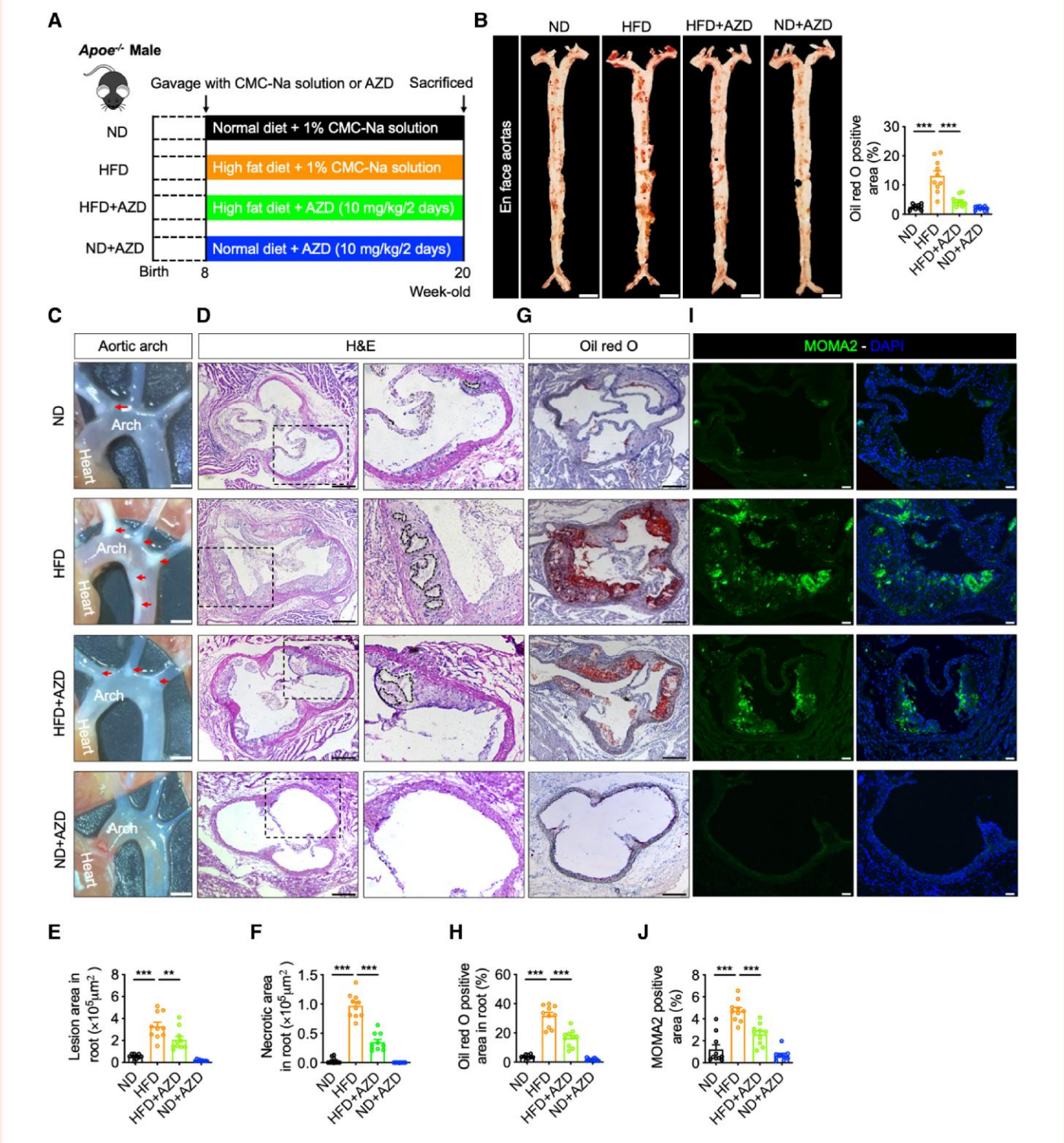

Figure 4 FGFR1 inhibition reduces HFD-induced AS in mice. (*A*) Male *Apoe*$^{-/-}$ mice were fed a HFD or ND for 12 weeks. A cohort in each group was treated with AZD4547 (AZD) for the duration of the study. Aortic and innominate arterial tissues were harvested and analysed. (*B*) Representative image and quantification of Oil Red O staining (*B*) of en face aortas from male *Apoe*$^{-/-}$ mice (scale bar = 2.5 mm; mean ± SEM; $n = 9$–10; ***$P < 0.001$). (*C*–*H*) Gross aortic arch (*C*, scale bar = 1 mm), representative H&E and quantification of lesion area and necrotic areas (*D*–*F*), representative Oil Red O–stained sections (*G*), and measurement of Oil Red O staining (*H*) are shown (scale bar = 250 μm; mean ± SEM; $n = 9$–10; **$P < 0.01$, ***$P < 0.001$). (*I* and *J*) Immunostaining of aortic root tissues of male *Apoe*$^{-/-}$ mice for monocyte/macrophage marker MOMA2. Tissues were counterstained with DAPI (scale bar = 250 μm). Quantification of immunoreactivity is shown as positively stained area (as %; mean ± SEM; $n = 9$–10; ***$P < 0.001$). One-way ANOVA followed by Bonferroni's *post hoc* test for (*B*), (*E*), (*F*), (*H*), and (*J*).

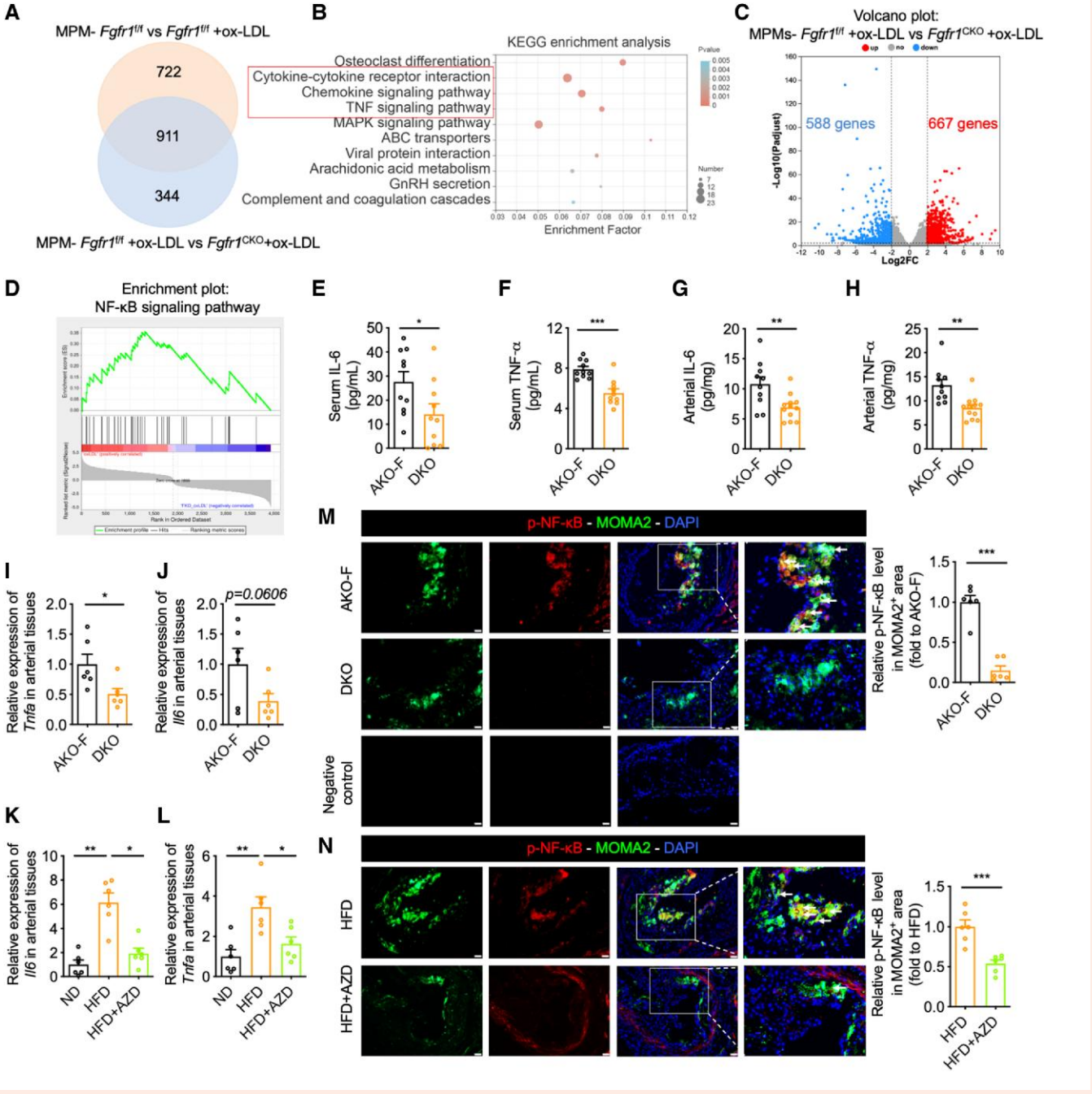

Figure 5 Myeloid-specific *Fgfr1* deficiency reduces HFD-induced inflammatory responses in mice. (*A* and *B*) MPMs were harvested from $Fgfr1^{f/f}$ and $Fgfr1^{CKO}$ mice. Cells were exposed to 50 μg/mL ox-LDL for 12 h, and RNA was sequenced. Figure showing a Venn plot (*A*) and KEGG enrichment analysis (*B*). Inflammatory factor enrichment is shown in coloured box in (*B*). (*C* and *D*) Figure showing volcano (*C*) and GSEA (*D*) plot from RNA-seq data. (*E* and *F*) Levels of circulating inflammatory factors IL-6 (*E*) and TNF-α (*F*) were measured in male AKO-F and DKO mice fed a HFD for 12 weeks (mean ± SEM; $n = 10$; $^{*}P < 0.05$, $^{***}P < 0.001$). (*G* and *H*) The protein levels of arterial inflammatory factors IL-6 (*G*) and TNF-α (*H*) were measured in male AKO-F and DKO mice fed a HFD for 12 weeks. Target protein levels were normalized to total tissue protein (mean ± SEM; $n = 10$; $^{**}P < 0.01$). (*I* and *J*) The mRNA levels of arterial inflammatory factors *Tnfa* (*I*) and *Il6* (*J*) were measured in male AKO-F and DKO mice fed a HFD for 12 weeks. Target mRNA levels were normalized to *Actb* (mean ± SEM; $n = 6$; $^{*}P < 0.05$). (*K* and *L*) mRNA levels of arterial tissue inflammatory factors *Il6* (*K*) and *Tnfa* (*L*) were measured in male $Apoe^{-/-}$ mice fed a ND, HFD, or HFD with AZD4547 treatment for 12 weeks. mRNA levels were normalized to *Actb* (mean ± SEM; $n = 6$; $^{*}P < 0.05$, $^{**}P < 0.01$). (*M*) Immunostaining of aortic root tissues from AKO-F and DKO mice fed a HFD for 12 weeks for MOMA2 and phosphorylated NF-κB p65. Tissues were counterstained with DAPI (scale bar = 50 μm). Quantification is shown on the right (mean ± SEM; $n = 6$; $^{***}P < 0.001$). (*N*) Immunostaining of aortic root tissues from male $Apoe^{-/-}$ mice fed a HFD or a HFD with AZD4547 treatment for 12 weeks for MOMA2 and phosphorylated NF-κB p65. Tissues were counterstained with DAPI (scale bar = 50 μm). Quantification is shown on the right (mean ± SEM; $n = 6$; $^{***}P < 0.001$). Student's *t*-test (unpaired, two-tailed) for (*E–J*), (*M*), and (*N*). One-way ANOVA followed by Bonferroni's *post hoc* test for (*K*) and (*L*).

cytokine levels were mirrored in protein and mRNA measurements for IL-6 and TNF-α in arterial tissues harvested from mice (*Figure 5G* and *J*). We confirmed these results in *Apoe*$^{-/-}$ mice fed a HFD and treated with AZD4547. AZD4547 prevented HFD-induced *Il6* and *Tnfa* expression (*Figure 5K* and *L*). We also examined the levels of chemokines and adhesion factors. Myeloid *Fgfr1* deletion reduced the mRNA expression of *Mcp1* and *Vcam1* and the protein expression of VCAM-1 in arterial tissues of *Apoe*$^{-/-}$ HFD mice (see Supplementary material online, *Figure S7A–D*), without influences on Ki67 level in macrophages (see Supplementary material online, *Figure S7E and F*), indicating that myeloid *Fgfr1* deletion reduced macrophage infiltration, rather than macrophage proliferation, in mouse atherosclerotic plaques. As NF-κB is a classical and obligatory transcriptional factor regulating inflammatory gene expression, we hypothesized that FGFR1 regulates inflammation through activating NF-κB. We stained aortas for phosphorylated NF-κB p65 and showed that FGFR1 blockage, genetic and pharmacological, significantly decreases p-NF-κB levels in MOMA2-positive cells (*Figure 5M* and *N*). These results suggest that macrophage FGFR1 modulates NF-κB inflammatory responses in experimental AS.

3.5 FGFR1 induces NF-κB activation and inflammatory cytokines through PLCγ

To investigate the mechanisms by which FGFR1 modulates NF-κB and inflammatory reactions, we exposed MPMs from *Fgfr1*$^{f/f}$ mice to 50 μg/mL ox-LDL for 5 or 15 min and probed for FGFR1 activation. Levels of phospho-FGFR1 increased rapidly in cells indicating that ox-LDL can activate FGFR1 signalling (*Figure 6A*). Two of the well-known downstream signalling mediators, PLCγ[29] and FRS2,[30] were also phosphorylated in MPMs exposed to ox-LDL (*Figure 6A* and *B*). Associated with ox-LDL–induced FGFR1 activity, we noted increased expression of inflammatory factors in MPMs (*Figure 6C–H*) and PLCγ (see Supplementary material online, *Figure S8A*) and NF-κB phosphorylation (*Figure 6I*). These inductions were not seen in cells isolated from *Fgfr1*^{CKO} mice (*Figure 6C–I*). Furthermore, inhibition of FGFR1 by AZD4547 in MPMs harvested from WT mice also suppressed ox-LDL–induced inflammatory factors (see Supplementary material online, *Figure S8B–E*). These results show that FGFR1 may mediate ox-LDL–induced NF-κB activation and inflammatory responses in macrophages. We then investigated whether PLCγ or FRS2 was required for ox-LDL-FGFR1 to induce inflammatory responses in macrophages. We knocked down the expression of PLCγ and FRS2 in RAW264.7 macrophages (*Figure 6J* and *K*) and then exposed the cells to 50 μg/mL ox-LDL. Interestingly, deficiency in PLCγ but not FRS2 prevented NF-κB p65 phosphorylation upon ox-LDL exposure (*Figure 6L* and *M*) and reduced the levels of inflammatory factor expression (*Figure 6P*). These studies suggest that FGFR1 signalling through PLCγ is required in macrophages to induce inflammatory factors in response to ox-LDL.

3.6 FGFR1 stimulates uptake of ox-LDL in macrophages

Lastly, we determined whether macrophage FGFR1 activity was involved in the uptake/phagocytosis of ox-LDL. MPMs from *Fgfr1*$^{f/f}$ and *Fgfr1*^{CKO} mice were exposed to 100 μg/mL ox-LDL for 24 h, and intracellular lipid accumulation was assessed by Oil Red O staining of cells. Increased Oil Red O staining was seen in MPMs from *Fgfr1*$^{f/f}$ but not from *Fgfr1*^{CKO} mice upon ox-LDL exposure (*Figure 7A* and *B*). We confirmed these results with exposure of MPMs to Dil-labelled ox-LDL and immunofluorescence staining (*Figure 7C* and *D*). Pharmacological inhibition of FGFR1 by AZD4547 suppressed ox-LDL uptake in WT MPMs (*Figure 7E* and *F*). The phagocytosed ox-LDL appeared as punctate Dil-ox-LDL label, which co-localized to clathrin, an important regulator of the endocytic pathway (*Figure 7G* and *H*). Pre-treatment of cells with AZD4547 reduced intracellular Dil-ox-LDL labelling. Assessment of ApoB and FGFR1 interaction by co-immunoprecipitation suggested that ox-LDL may not bind to FGFR1 (see Supplementary material online, *Figure S9A*), indicating that FGFR1 may regulate phagocytosis of ox-LDL instead. We examined the expression of scavenger receptor CD36 in aortic tissues isolated from AKO-F and DKO mice. The levels of *Cd36* were significantly reduced in DKO mice fed a HFD compared with AKO-F mice (see Supplementary material online, *Figure S9B*). The levels of *Scarb1*, *Abca1*, and *Abcg1*, however, were not altered in DKO mice (see Supplementary material online, *Figure S9B*). Moreover, *Cd36* levels were reduced in MPMs from *Fgfr1*^{CKO} upon ox-LDL exposure compared with MPMs from *Fgfr1*$^{f/f}$ mice, but no differences were noted in *Scarb1*, *Abca1*, and *Abcg1* levels (see Supplementary material online, *Figure S9C*). CD36 protein levels also showed an increase in *Fgfr1*$^{f/f}$ MPMs upon ox-LDL exposure but not in MPMs harvested from *Fgfr1*^{CKO} mice (see Supplementary material online, *Figure S9D*). The results show that macrophages uptake ox-LDL in a FGFR1/CD36-dependent manner.

4. Discussion

The key findings of our study are that (i) atherosclerotic lesions show elevated FGFR1 and *Fgfr1* deficiency in myeloid cells significantly reduces aortic tissue inflammatory reactions, lipid accumulation, and lesions in *Apoe*$^{-/-}$ mice maintained on a HFD; (ii) ox-LDL activates FGFR1 in macrophages to induce the expression of inflammatory cytokines and chemokines; and (iii) FGFR1 activity leads to PLCγ and NF-κB activation and ox-LDL uptake in macrophages. Together, these results provide evidence of a novel FGFR1 signalling mechanism in atheromatous growth.

FGFR1 plays a critical role during growth and development. Aberrant FGFR1, through overexpression and mutations, are also linked to carcinogenesis.[31,32] In addition, activation of FGFR1 has been implicated in a host of cardiovascular and inflammatory diseases.[15–20] For example, blocking FGFR1 improves left ventricular hypertrophy and function in nephrectomy rats,[17] and overexpression of FGFR1 in cardiomyocytes causes hypertrophic cardiomyopathy.[16] In terms of inflammatory conditions, FGFR1 is implicated in acute septic injury[18–20] through disruption of lipopolysaccharide signalling and injury. Pharmacological inhibition of FGFR1 suppresses inflammatory responses and shock in septic mice.[19] Activating FGFR1 also results in the amplification of inflammatory responses[33] and increases the level of TNF production.[34] In AS, previous reports had shown expression of FGFR1 in macrophages within human atheromas.[22] Treatment of *Apoe*$^{-/-}$ mice with SU5402 significant reduced atheroma generation induced by HFD.[24] However, SU5402 is known to inhibit disparate signalling pathways.[35] A more recent study used a specific allosteric FGFR1 inhibitor SSR128129E in *Apoe*$^{-/-}$ mice maintained on ND for up to 5 months and showed reduced spontaneous lesions.[36] Although AS was not the primary focus of the study by Dol-Gleizes *et al.*[36] or examined in detail, it did provide supporting evidence that FGFR1 is involved.

Our results confirm the elevated levels of macrophage FGFR1 in human and experimental atherosclerotic lesions. One possibility for the apparent increase in FGFR1 in aortic plaques is that infiltrating monocytes may be the major contributors to the increased expression. Indeed, we show that FGFR1 primarily localizes to CD68-positive macrophages in atherosclerotic lesions. Our *in vitro* data show that ox-LDL challenge did not induce FGFR1 expression in macrophages. These results indicate that increased FGFR1 in atherosclerotic lesions may come from the increased monocyte infiltration. HFD feeding of mice *in vivo* or ox-LDL challenge of MPMs *in vitro* induces FGFR1 phosphorylation, indicating FGFR1 activation to atherosclerotic lesion development. These ideas promoted us to generate and examine myeloid-specific *Fgfr1*-deficient mice and to test whether pharmacological inhibitor of FGFR1 prevents AS. We report that myeloid *Fgfr1*-deficient mice are remarkably protected against HFD-induced lesions in the aorta, as well as towards lipid accumulation, inflammatory cytokine expression, and immune cell infiltration. Systemic treatment of mice with AZD4547 also prevented atherosclerotic lesions in mice. Although previous studies have implicated FGFR1 in inflammatory systems,[18–20] we provide empirical evidence of specific macrophage-derived FGFR1 in AS through the regulation of inflammatory responses.

FGFR1 activates a wide range of downstream signalling proteins including Rho GTPases, mitogen-activated protein kinases, protein kinases B and

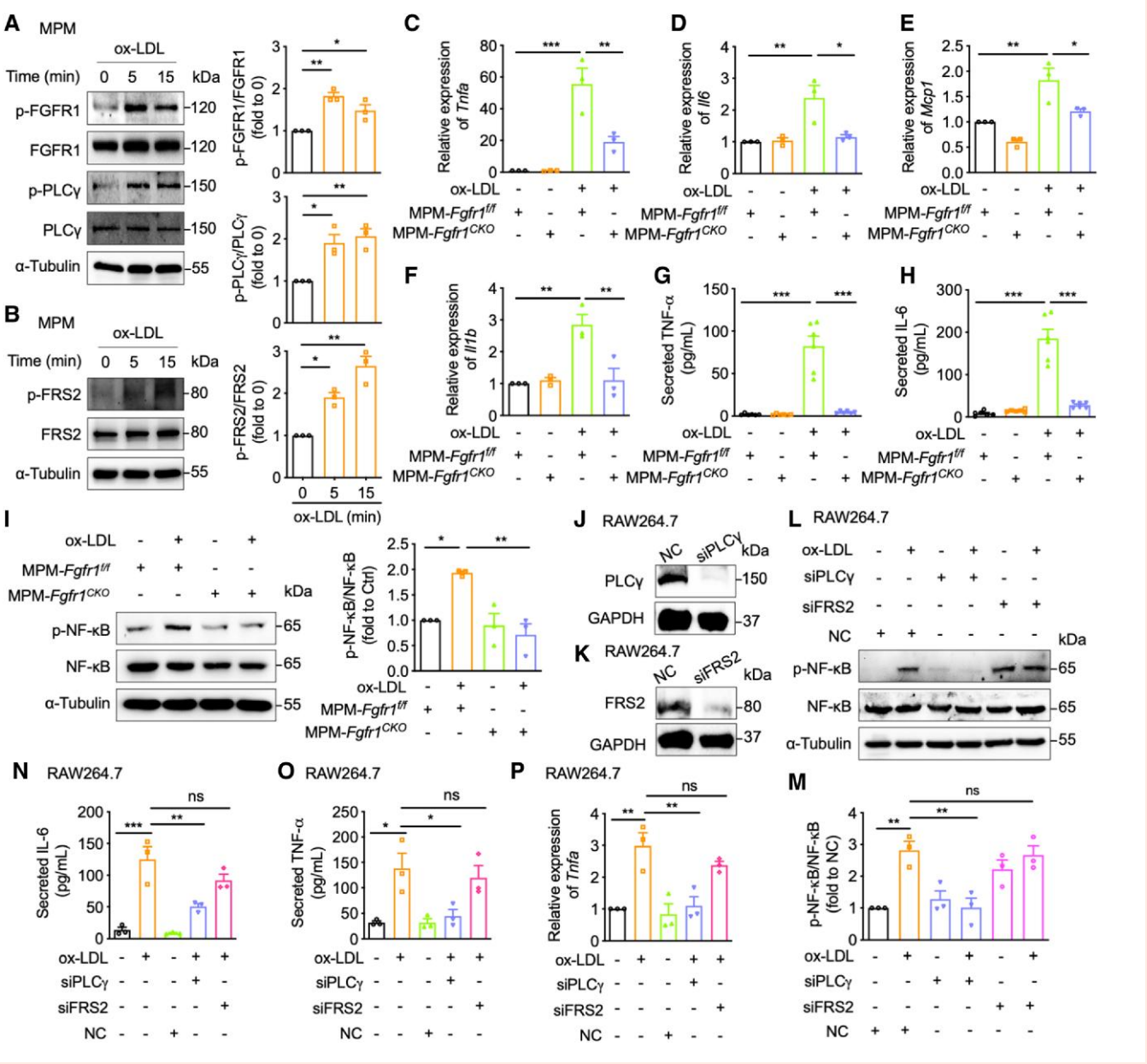

Figure 6 Ox-LDL induces inflammatory cytokines in macrophages through FGFR1 and PLCγ. (*A* and *B*) MPMs were harvested from *Fgfr1*$^{f/f}$ mice and cultured with 50 μg/mL ox-LDL for indicated time points. Immunoblotting was performed to assess phosphorylation of FGFR1, FRS2, and PLCγ. Representative blots and quantification are shown. α-Tubulin and total proteins were used as controls (mean ± SEM; $n = 3$; *$P < 0.05$, **$P < 0.01$). (*C–F*) MPMs harvested from *Fgfr1*$^{f/f}$ and *Fgfr1*^{CKO} mice and exposed to 50 μg/mL ox-LDL for 24 h. mRNA levels of inflammatory factors were measured. *Actb* was used for normalization (mean ± SEM; $n = 3$; *$P < 0.05$, **$P < 0.01$, ***$P < 0.001$). (*G* and *H*) Levels of TNF-α and IL-6 proteins in cell culture media. Cells were treated as indicated in (*C–F*) [mean ± SEM; $n = 6$; ***$P < 0.001$]. (*I*) MPMs from *Fgfr1*$^{f/f}$ and *Fgfr1*^{CKO} mice were exposed to 50 μg/mL ox-LDL for 15 min. Levels of phospho-NF-κB p65 were measured by immunoblotting. Representative blots and quantification are shown. α-Tubulin was used as loading control (mean ± SEM; $n = 3$; *$P < 0.05$, **$P < 0.01$). (*J* and *K*) RAW264.7 cells were transfected with siRNA against *Plcg1* (*J*) and *Frs2* (*K*). Scrambled sequences were used as NC. Knockdown efficiency was measured by immunoblotting. GAPDH was used as loading control. (*L* and *M*) RAW264.7 cells transfected with *Plcg1* or *Frs2* siRNA were exposed to 50 μg/mL ox-LDL for 15 min. Levels of phospho-NF-κB p65 were measured by immunoblotting. Representative blots and quantification are shown. α-Tubulin was used as loading control (mean ± SEM; $n = 3$; **$P < 0.01$). (*N–P*) RAW264.7 cells with *Plcg1* or *Frs2* knocked down were exposed to 50 μg/mL ox-LDL for 24 h. Inflammatory factor expression was measured. Target protein levels were normalized to total protein measurement from cultures (*N* and *O*), and mRNA (*P*) was normalized to *Actb* (mean ± SEM; $n = 3$; *$P < 0.05$, **$P < 0.01$, ***$P < 0.001$). One-way ANOVA followed by Bonferroni's *post hoc* test for (*A–I*) and (*M–P*). ns, not significant.

C, and NF-κB.[37,38] Though it is not clear from our study as to how ox-LDL activates FGFR1, we did find that the eventual NF-κB activation was differentially regulated by SH2-binding signalling intermediates of FGFR1. Specifically, we found that downstream of ox-LDL-FGFR1 activation, only *Plcg1* promoted the production of inflammatory cytokines by macrophages. Knockdown of *Frs2* did not reduce inflammatory cytokines or NF-κB activation following ox-LDL exposure of macrophages. This may implicate secondary mediators of PLCγ pathway[37] (diacylglycerol, inositol

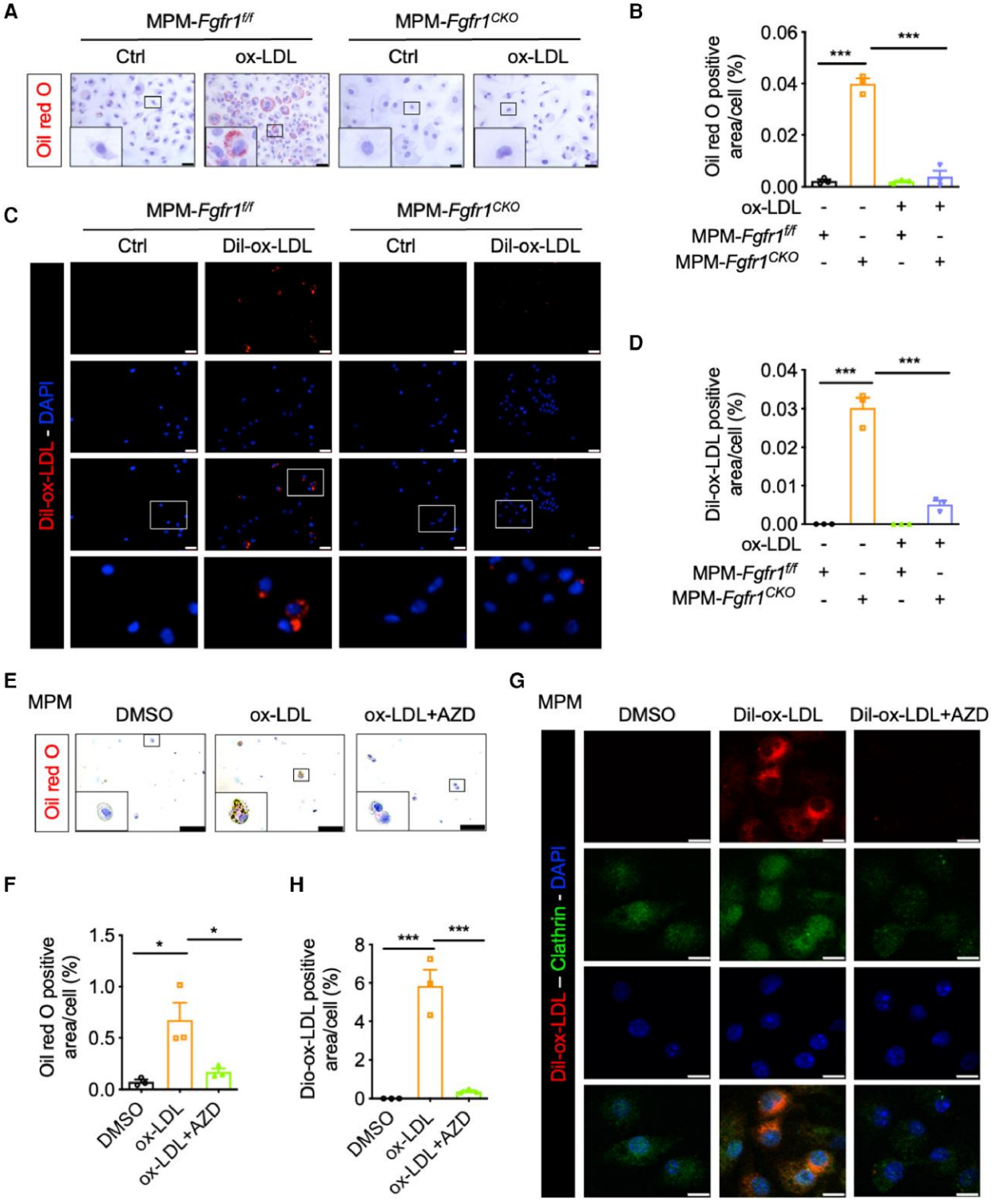

Figure 7 Myeloid FGFR1 is required for ox-LDL uptake. (*A* and *B*) MPMs from *Fgfr1*$^{f/f}$ and *Fgfr1*^{CKO} mice were exposed to 100 μg/mL ox-LDL for 24 h. Lipid accumulation in cells was measured by staining for Oil Red O. Cells were counterstained with haematoxylin (*A*; scale bar = 50 μm). Quantification of Oil Red O staining is shown in (*B*) [mean ± SEM; $n = 3$; ***$P < 0.001$]. (*C* and *D*) MPMs from *Fgfr1*$^{f/f}$ and *Fgfr1*^{CKO} mice were exposed to 50 μg/mL Dil-ox-LDL for 24 h. Cells were counterstained with DAPI and immunofluorescence images were taken (*C*; scale bar = 25 μm). Quantification of Dil-ox-LDL staining is shown in (*D*) [mean ± SEM; $n = 3$; ***$P < 0.001$]. (*E* and *F*) MPMs from WT mice were pre-treated with 10 μM AZD4547 for 1 h. Cells were then exposed to 100 μg/mL ox-LDL for 24 h. Lipid accumulation was detected by Oil Red O staining (*E*; scale bar = 75 μm). Quantification of Oil Red O staining is shown in (*F*) [mean ± SEM; $n = 3$; *$P < 0.05$]. (*G* and *H*) MPMs from WT mice were pre-treated with 10 μM AZD4547 for 1 h and then exposed to 50 μg/mL Dil-ox-LDL for 24 h. Cells were counterstained with DAPI, and immunofluorescence images were taken (*G*; scale bar = 10 μm). Quantification of Dil-ox-LDL uptake is shown in (*H*) [mean ± SEM; $n = 3$; ***$P < 0.001$]. One-way ANOVA followed by Bonferroni's *post hoc* test for (*B*), (*D*), (*F*), and (*H*).

triphosphate, intracellular calcium, and protein kinase C) in ox-LDL–mediated inflammatory reactions. Elucidation of both upstream (ox-LDL–mediated FGFR1 activation) and downstream (PLCγ-mediated NF-κB activation) secondary messengers in inflammatory AS would be critical for future studies.

Although we focused on FGFR1 signalling in macrophages, it is important to acknowledge that FGFR1 signalling in other cell types may participate in AS. The scRNA-seq data and immunostaining analysis also found FGFR1 expression in endothelial cells and SMCs. Previous studies have hinted at important FGFR1 signalling in both endothelial and SMC alterations.[39,40] Endothelial cell–specific knockout of FGFR1 leads to activation of transforming growth factor β signalling and endothelial-to-mesenchymal transition in mice.[41] In endothelial cells, angiogenic FGFR1 activity[42] may also alter macrophage numbers.[43] Similarly, FGFR1 activity has been reported to regulate the proliferation of SMCs.[39,44,45] Although our data showed that myeloid FGFR1 deficiency did not affect the phenotypic switching of SMCs, studies examining the role of FGFR1 in other cell types related to AS are interesting and deserve further investigation in the future.

Another issue worth investigating is the impact of FGFR1 in other tissues. Our data show that systemic FGFR1 inhibition by AZD4547 reduces body weight gain and serum lipid levels in mice fed a HFD (see Supplementary material online, *Figure S5I–L*). These changes were not observed in myeloid-specific *Fgfr1*-deficient mice a HFD (*Figure 2C–G*). These data indicated that inhibition of FGFR1 in other tissues (e.g. liver and adipose tissue) by AZD4547 may affect lipid metabolism in mice, which is in line with evidence generated from other systems. It has been reported that activation of FGF1/FGFR1 signalling pathway promotes adipogenesis.[46] Using FGFR1 inhibitor treatment and specific FGFR1 knockdown in adipocytes, another study revealed a role for FGFR1 in adipogenesis and identified FGFR1 as a potential therapeutic target to reduce obesity.[47] Also, antibody-mediated FGFR1 neutralization increased glucose uptake in white and brown adipose tissue to protect mice from diet-induced obesity[48] and reduced body weight gain.[49] In addition, silencing *Fgfr1* expression blocked free fatty acid–induced lipid accumulation in mouse hepatocytes.[50] These studies suggest that pharmacological inhibition of FGFR1 may have broader protection against HFD-induced AS, highlighting the advantage of FGFR1 inhibitor in the therapy of AS-related disease.

In summary, we have provided direct evidence of a novel FGFR1–PLCγ–NF-κB signalling mechanism in the promotion of atheromatous growth. We demonstrated that *Fgfr1* deletion in myeloid cells of *Apoe*-deficient mice affords protection against HFD-induced atherosclerotic lesions, lipid accumulation, and inflammatory reactions. In macrophage culture studies, we show that ox-LDL induces inflammatory factors through FGFR1 and PLCγ. Although our mechanistic studies point to macrophage-driven FGFR1 activity as the culprit, broad inhibition of FGFR1 likely is as effective in reducing atherogenesis. AZD4547 and other emerging inhibitors of FGFR1 are potentially therapeutic agents, particularly since these are already in Phase I and II clinical trials for cancer treatment.[51]

Translational perspective

Atherosclerosis is a chronic inflammatory disease with high morbidity and mortality rates worldwide. This study shows that either myeloid *Fgfr1* deficiency or pharmacological FGFR1 inhibitor reduces aortic tissue inflammatory reactions, lipid accumulation, and atherosclerotic lesions by inhibiting PLCγ–NF-κB activation and oxidized LDL uptake in macrophages. Small-molecule FGFR1 inhibitors have already been used in the clinic for cancer treatment. Therefore, our study provides evidence of a novel FGFR1 signalling mechanism in atherosclerosis and sheds new light on the application of FGFR1 inhibitors as potential therapeutic agents for treating atherosclerosis-related diseases.

Supplementary material

Supplementary material is available at *Cardiovascular Research* online.

Authors' contributions

C.He. and G.L. contributed to the literature search and study design. L.W. and G.L. participated in the drafting of the article. L.W., S.Z., J.Z., L.H., Y.S., L.G., B.W., X.N., C.Hu., and X.H. carried out the experiments. G.L., B.X., and C.He. revised the manuscript. L.W. and W.L. contributed to data collection and analysis.

Conflict of interest: none declared.

Funding

This study was supported by the National Natural Science Foundation of China (81930108 to G.L.).

Data availability

The data underlying this article will be shared on reasonable request to the corresponding author.

References

1. Murray CJ, Lopez AD. Measuring the global burden of disease. *N Engl J Med* 2013;**369**:448–457.
2. Libby P, Ridker PM, Hansson GK. Progress and challenges in translating the biology of atherosclerosis. *Nature* 2011;**473**:317–325.
3. Susser LI, Rayner KJ. Through the layers: how macrophages drive atherosclerosis across the vessel wall. *J Clin Invest* 2022;**132**:e157011.
4. Geovanini GR, Libby P. Atherosclerosis and inflammation: overview and updates. *Clin Sci (Lond)* 2018;**132**:1243–1252.
5. Libby P. Inflammation in atherosclerosis. *Arterioscler Thromb Vasc Biol* 2012;**32**:2045–2051.
6. Doran AC. Inflammation resolution: implications for atherosclerosis. *Circ Res* 2022;**130**:130–148.
7. Yamaguchi TP, Harpal K, Henkemeyer M, Rossant J. fgfr-1 is required for embryonic growth and mesodermal patterning during mouse gastrulation. *Genes Dev* 1994;**8**:3032–3044.
8. Niu Z, Jin R, Zhang Y, Li H. Signaling pathways and targeted therapies in lung squamous cell carcinoma: mechanisms and clinical trials. *Signal Transduct Target Ther* 2022;**7**:353.
9. Labanca E, Yang J, Shepherd PDA, Wan X, Starbuck MW, Guerra LD, Anselmino N, Bizzotto JA, Dong J, Chinnaiyan AM, Ravoori MK, Kundra V, Broom BM, Corn PG, Troncoso P, Gueron G, Logothethis CJ, Navone NM. Fibroblast growth factor receptor 1 drives the metastatic progression of prostate cancer. *Eur Urol Oncol* 2022;**5**:164–175.
10. Sternberg CN, Petrylak DP, Bellmunt J, Nishiyama H, Necchi A, Gurney H, Lee JL, van der Heijden MS, Rosenbaum E, Penel N, Pang ST, Li JR, García Del Muro X, Joly F, Pápai Z, Bao W, Ellinghaus P, Lu C, Sierecki M, Coppieters S, Nakajima K, Ishida TC, Quinn DI. FORT-1: phase II/III study of rogaratinib versus chemotherapy in patients with locally advanced or metastatic urothelial carcinoma selected based on FGFR1/3 mRNA expression. *J Clin Oncol* 2023;**41**:629–639.
11. Coombes RC, Badman PD, Lozano-Kuehne JP, Liu X, Macpherson IR, Zubairi I, Baird RD, Rosenfeld N, Garcia-Corbacho J, Cresti N, Plummer R, Armstrong A, Allerton R, Landers D, Nicholas H, McLellan L, Lim A, Mouliere F, Pardo OE, Ferguson V, Seckl MJ. Results of the phase IIa RADICAL trial of the FGFR inhibitor AZD4547 in endocrine resistant breast cancer. *Nat Commun* 2022;**13**:3246.
12. Lassman AB, Sepulveda-Sanchez JM, Cloughesy TF, Gil-Gil MJ, Puduvalli VK, Raizer JJ, De Vos FYF, Wen PY, Butowski NA, Clement PMJ, Groves MD, Belda-Iniesta C, Giglio P, Soifer HS, Rowsey S, Xu C, Avogadri F, Wei G, Moran S, Roth P. Infigratinib in patients with recurrent gliomas and FGFR alterations: a multicenter phase II study. *Clin Cancer Res* 2022;**28**:2270–2277.
13. Meric-Bernstam F, Bahleda R, Hierro C, Sanson M, Bridgewater J, Arkenau HT, Tran B, Kelley RK, Park JO, Javle M, He Y, Benhadji KA, Goyal L. Futibatinib, an irreversible FGFR1-4 inhibitor, in patients with advanced solid tumors harboring FGF/FGFR aberrations: a phase I dose-expansion study. *Cancer Discov* 2022;**12**:402–415.

14. Xu Z, Luo W, Chen L, Zhuang Z, Yang D, Qian J, Khan ZA, Guan X, Wang Y, Li X, Liang G. Ang II (angiotensin II)-induced FGFR1 (fibroblast growth factor receptor 1) activation in tubular epithelial cells promotes hypertensive kidney fibrosis and injury. *Hypertension* 2022;**79**:2028–2041.
15. Zheng Y, Ma H, Hu E, Huang Z, Cheng X, Xiong C. Inhibition of FGFR signaling with PD173074 ameliorates monocrotaline-induced pulmonary arterial hypertension and rescues BMPR-II expression. *J Cardiovasc Pharmacol* 2015;**66**:504–514.
16. Cilvik SN, Wang JI, Lavine KJ, Uchida K, Castro A, Gierasch CM, Weinheimer CJ, House SL, Kovacs A, Nichols CG, Ornitz DM. Fibroblast growth factor receptor 1 signaling in adult cardiomyocytes increases contractility and results in a hypertrophic cardiomyopathy. *PLoS One* 2013;**8**:e82979.
17. Di Marco GS, Reuter S, Kentrup D, Grabner A, Amaral AP, Fobker M, Stypmann J, Pavenstadt H, Wolf M, Faul C, Brand M. Treatment of established left ventricular hypertrophy with fibroblast growth factor receptor blockade in an animal model of CKD. *Nephrol Dial Transplant* 2014;**29**:2028–2035.
18. Lou D, Han J, Zhou L, Ma H, Xv J, Shou J, Xu Z, Jiang L, Qian Y. Fibroblast growth factor receptor 1 antagonism attenuates lipopolysaccharide-induced activation of hepatic stellate cells via suppressing inflammation. *Exp Ther Med* 2018;**16**:2909–2916.
19. Huang Y, Wang F, Li H, Xu S, Xu W, Pan X, Hu Y, Mao L, Qian S, Pan J. Inhibition of fibroblast growth factor receptor by AZD4547 protects against inflammation in septic mice. *Inflammation* 2019;**42**:1957–1967.
20. Chen X, Zhang X, Xu J, Zhao Y, Bao J, Zheng Z, Han J. AZD4547 attenuates lipopolysaccharide-induced acute kidney injury by inhibiting inflammation: the role of FGFR1 in renal tubular epithelial cells. *Drug Des Devel Ther* 2020;**14**:833–844.
21. Hughes SE, Crossman D, Hall PA. Expression of basic and acidic fibroblast growth factors and their receptor in normal and atherosclerotic human arteries. *Cardiovasc Res* 1993;**27**: 1214–1219.
22. Brogi E, Winkles JA, Underwood R, Clinton SK, Alberts GF, Libby P. Distinct patterns of expression of fibroblast growth factors and their receptors in human atheroma and nonatherosclerotic arteries. Association of acidic FGF with plaque microvessels and macrophages. *J Clin Invest* 1993;**92**:2408–2418.
23. Hughes SE. Localisation and differential expression of the fibroblast growth factor receptor (FGFR) multigene family in normal and atherosclerotic human arteries. *Cardiovasc Res* 1996; **32**:557–569.
24. Raj T, Kanellakis P, Pomilio G, Jennings G, Bobik A, Agrotis A. Inhibition of fibroblast growth factor receptor signaling attenuates atherosclerosis in apolipoprotein E-deficient mice. *Arterioscler Thromb Vasc Biol* 2006;**26**:1845–1851.
25. Gavine PR, Mooney L, Kilgour E, Thomas AP, Al-Kadhimi K, Beck S, Rooney C, Coleman T, Baker D, Mellor MJ, Brooks AN, Klinowska T. AZD4547: an orally bioavailable, potent, and selective inhibitor of the fibroblast growth factor receptor tyrosine kinase family. *Cancer Res* 2012;**72**:2045–2056.
26. Pan Y, Zhu G, Wang Y, Cai L, Cai Y, Hu J, Li Y, Yan Y, Wang Z, Li X, Wei T, Liang G. Attenuation of high-glucose-induced inflammatory response by a novel curcumin derivative B06 contributes to its protection from diabetic pathogenic changes in rat kidney and heart. *J Nutr Biochem* 2013;**24**:146–155.
27. Piedrahita JA, Zhang SH, Hagaman JR, Oliver PM, Maeda N. Generation of mice carrying a mutant apolipoprotein E gene inactivated by gene targeting in embryonic stem cells. *Proc Natl Acad Sci U S A* 1992;**89**:4471–4475.
28. Tucker JA, Klein T, Breed J, Breeze AL, Overman R, Phillips C, Norman RA. Structural insights into FGFR kinase isoform selectivity: diverse binding modes of AZD4547 and ponatinib in complex with FGFR1 and FGFR4. *Structure* 2014;**22**:1764–1774.
29. Vainikka S, Joukov V, Wennstrom S, Bergman M, Pelicci PG, Alitalo K. Signal transduction by fibroblast growth factor receptor-4 (FGFR-4). Comparison with FGFR-1. *J Biol Chem* 1994; **269**:18320–18326.
30. Zhang Y, McKeehan K, Lin Y, Zhang J, Wang F. Fibroblast growth factor receptor 1 (FGFR1) tyrosine phosphorylation regulates binding of FGFR substrate 2alpha (FRS2alpha) but not FRS2 to the receptor. *Mol Endocrinol* 2008;**22**:167–175.
31. Wei H, Hou J, Pan J, Su X, Li L, Wang X, Chen Z. A sarcoidosis-like granuloma reaction in the lymph nodes of a patient with lung squamous cancer: from stasis to the invasive phase with FGFR1 gene amplification. *Clin Respir J* 2016;**10**:530–534.
32. Katoh M, Nakagama H. FGF receptors: cancer biology and therapeutics. *Med Res Rev* 2014; **34**:280–300.
33. Fitzpatrick EA, Han X, Xiao Z, Quarles LD. Role of fibroblast growth factor-23 in innate immune responses. *Front Endocrinol (Lausanne)* 2018;**9**:320.
34. Han X, Li L, Yang J, King G, Xiao Z, Quarles LD. Counter-regulatory paracrine actions of FGF-23 and 1,25(OH)2 D in macrophages. *FEBS Lett* 2016;**590**:53–67.
35. Sun L, Tran N, Liang C, Tang F, Rice A, Schreck R, Waltz K, Shawver LK, McMahon G, Tang C. Design, synthesis, and evaluations of substituted 3-[(3- or 4-carboxyethylpyrrol-2-yl) methylidenyl]indolin-2-ones as inhibitors of VEGF, FGF, and PDGF receptor tyrosine kinases. *J Med Chem* 1999;**42**:5120–5130.
36. Dol-Gleizes F, Delesque-Touchard N, Mares AM, Nestor AL, Schaeffer P, Bono F. A new synthetic FGF receptor antagonist inhibits arteriosclerosis in a mouse vein graft model and atherosclerosis in apolipoprotein E-deficient mice. *PLoS One* 2013;**8**:e80027.
37. Nies VJ, Sancar G, Liu W, van Zutphen T, Struik D, Yu RT, Atkins AR, Evans RM, Jonker JW, Downes MR. Fibroblast growth factor signaling in metabolic regulation. *Front Endocrinol (Lausanne)* 2015;**6**:193.
38. Xie Y, Zinkle A, Chen L, Mohammadi M. Fibroblast growth factor signalling in osteoarthritis and cartilage repair. *Nat Rev Rheumatol* 2020;**16**:547–564.
39. Chen PY, Qin L, Li G, Tellides G, Simons M. Smooth muscle FGF/TGFbeta cross talk regulates atherosclerosis progression. *EMBO Mol Med* 2016;**8**:712–728.
40. Chen PY, Qin L, Baeyens N, Li G, Afolabi T, Budatha M, Tellides G, Schwartz MA, Simons M. Endothelial-to-mesenchymal transition drives atherosclerosis progression. *J Clin Invest* 2015; **125**:4514–4528.
41. Chen PY, Qin L, Tellides G, Simons M. Fibroblast growth factor receptor 1 is a key inhibitor of TGFbeta signaling in the endothelium. *Sci Signal* 2014;**7**:ra90.
42. Tanghetti E, Ria R, Dell'Era P, Urbinati C, Rusnati M, Ennas MG, Presta M. Biological activity of substrate-bound basic fibroblast growth factor (FGF2): recruitment of FGF receptor-1 in endothelial cell adhesion contacts. *Oncogene* 2002;**21**:3889–3897.
43. Moulton KS, Vakili K, Zurakowski D, Soliman M, Butterfield C, Sylvin E, Lo KM, Gillies S, Javaherian K, Folkman J. Inhibition of plaque neovascularization reduces macrophage accumulation and progression of advanced atherosclerosis. *Proc Natl Acad Sci U S A* 2003;**100**: 4736–4741.
44. Scata KA, Bernard DW, Fox J, Swain JL. FGF receptor availability regulates skeletal myogenesis. *Exp Cell Res* 1999;**250**:10–21.
45. Chen PY, Simons M, Friesel R. FRS2 via fibroblast growth factor receptor 1 is required for platelet-derived growth factor receptor beta-mediated regulation of vascular smooth muscle marker gene expression. *J Biol Chem* 2009;**284**:15980–15992.
46. Wang S, Cao S, Arhatte M, Li D, Shi Y, Kurz S, Hu J, Wang L, Shao J, Atzberger A, Wang Z, Wang C, Zang W, Fleming I, Wettschureck N, Honore E, Offermanns S. Adipocyte Piezo1 mediates obesogenic adipogenesis through the FGF1/FGFR1 signaling pathway in mice. *Nat Commun* 2020;**11**:2303.
47. Widberg CH, Newell FS, Bachmann AW, Ramnoruth SN, Spelta MC, Whitehead JP, Hutley LJ, Prins JB. Fibroblast growth factor receptor 1 is a key regulator of early adipogenic events in human preadipocytes. *Am J Physiol Endocrinol Metab* 2009;**296**:E121–E131.
48. Lewis JE, Samms RJ, Cooper S, Luckett JC, Perkins AC, Dunbar JD, Smith DP, Emmerson PJ, Adams AC, Ebling FJP, Tsintzas K. Antibody-mediated targeting of the FGFR1c isoform increases glucose uptake in white and brown adipose tissue in male mice. *Endocrinology* 2017;**158**:3090–3096.
49. Sun HD, Malabunga M, Tonra JR, DiRenzo R, Carrick FE, Zheng H, Berthoud HR, McGuinness OP, Shen J, Bohlen P, Leibel RL, Kussie P. Monoclonal antibody antagonists of hypothalamic FGFR1 cause potent but reversible hypophagia and weight loss in rodents and monkeys. *Am J Physiol Endocrinol Metab* 2007;**292**:E964–E976.
50. Wang XY, Lu LJ, Li YM, Xu CF. MicroRNA-376b-3p ameliorates nonalcoholic fatty liver disease by targeting FGFR1 and regulating lipid oxidation in hepatocytes. *Life Sci* 2022;**308**: 120925.
51. Dienstmann R, Rodon J, Prat A, Perez-Garcia J, Adamo B, Felip E, Cortes J, Iafrate AJ, Nuciforo P, Tabernero J. Genomic aberrations in the FGFR pathway: opportunities for targeted therapies in solid tumors. *Ann Oncol* 2014;**25**:552–563.